AC loss in Ag/Bi-2223 tapes in AC field

Mohammad Mehdi Farhoudi
University of Wollongong

AC Loss in Ag/Bi-2223 Tapes in AC Field

A thesis submitted in fulfilment of the requirements for the award of the degree

Honours Master of Engineering

from

University of Wollongong

by

Mohammad Mehdi Farhoudi (B.Sc.)

Institute of Superconducting and Electronic Materials

2002

Candidate's Certificate

This is to certify that the work presented in this thesis is original and was carried out by the candidate in the laboratories of Institute of Superconducting and Electronic Materials and the Department of Materials Engineering at the University of Wollongong, New South Wales, Australia, and has not been submitted for a degree to any other university or institution.

Mohammad Mehdi Farhoudi

Contents

List of Figures

List of Tables

Abstract

Bi-2223/Ag tapes are currently the only HTS that can be classified as “conductor”; i.e. long lengths of the tapes can be purchased and used in practical applications. They have started their use primarily in applications with alternating currents (AC), such as transformers, high current/low voltage cables, motors and generators.

The energy losses in practical superconductors are negligibly small under suitable working conditions. However, Bi-2223/Ag tapes are composite conductors, consisting of superconducting filaments in a silver matrix. Composite conductors are associated with additional losses when the tape is used in AC applications, commonly referred to AC coupling loss.

The susceptibility of different tapes to the coupling losses is usually described by effective transverse resistivity, $\rho_{\perp}$. $\rho_{\perp}$ differs from resistivity of the silver matrix, and it is a convenient way to describe the susceptibility of a tape to the AC loss. Coupling currents between the filaments flow in a complicated pattern because of the complex geometry of the tapes. The coupling current loss depends not only on the resistivity of the silver matrix, but also on the spatial distribution of the currents. Therefore, the overall shape of the tape, as well as the architecture of the superconducting filaments in the tape are important factors defining the coupling losses. The geometrical factor needs to be known for determination of $\rho_{\perp}$ and is for tapes usually taken simply as the aspect ratio of the tapes, *a/b*, where *a* is the thickness and *b* is the width of the tape. The

proposed study is aimed at determining the effective transverse resistivity of 8 filamentary untwisted Bi-2223/Ag tapes, fabricated by the PIT method and heat treated at 837^{o}C. This takes into account the filament configuration, tape thickness and width as well. Three thicknesses of 0.18mm, 0.24mm and 0.33mm tape were studied.

I_c, X-ray diffraction, and optical microscopy measurements were performed in order to characterise the tape. The Bi2223/Bi2212 phase ratio in the composite is X_{Bi2223}=~87%, and there is no bridging between the filament and no discontinuities. The I_c values for the thicknesses are: I_c(0.18mm)=11.2A, I_c(0.24mm)=17.85A, I_c(0.33mm)=13.8A. The I_c vs. thickness values demonstrate an optimum thickness for I_c.

Measurements of the frequency dependence of the AC loss makes it possible to obtain the value of $\rho_{\perp}$ for each thickness-length of tape. This measurement was performed using an induction method, with the excitation field applied parallel to the face of the tape. The $\rho_{\perp}$ is large, comparing to the tape matrix resistivity, ρ_{Ag}.

Chapter 1

Introduction

For many years, power utilities around the world have been testing a new generation of technologies that could revolutionise the way electricity is delivered from place to place. Based on unique materials discovered 15 years ago, High-Temperature Superconductors (HTS), these technologies are built around wires and cables made from the superconductors, which under the right conditions, allow electric current to flow through them virtually without resistance.

Already finding uses in small-scale electronic devices, these newest superconducting materials are poised to break into large-scale applications. Some applications are: (1) Magnet applications (e.g. MRI, NMR), (2) Electrical application (e.g. SMES, fly wheels, superconducting power cables, fault current limiters, superconducting generators, superconducting transformers, superconducting motors).

Today, with efforts to deregulate electrical utilities, the main users of HTS will be the power generating companies and distribution firms that not only have to match low prices, but also must guarantee the quality and reliability of the power they deliver. Also, improved performance and efficiency over conventional room-temperature devices are expected.

Use of superconducting Bi-2223 tapes in large-scale applications provides the ability to transport large direct current (DC) with no measurable resistive losses. DC is rarely used in the large-scale application sector, because early in the 20^{th} century it was realised that increasing voltage and reducing current could reduce losses in conventional cables. This transformation can only be done with alternating current (AC), and so the grid was built to operate with alternating current.

A practical tape must thus have current density with low losses (at high magnetic fields) compared to an ordinary Copper cable in order to be technologically useful. In other words the AC loss of the tape should be as low as possible.

The low temperature superconductors (LTS) that operate in liquid Helium easily satisfy this requirement, however LTS are compromised by the costly and technologically complicated requirement for liquid Helium. Consequently, utilities or end-users did not accept it on a large scale.

The 1986 discovery of high temperature superconductors (HTS) provided a new impetus for pursuing superconducting large-scale applications because HTS can operate at liquid Nitrogen temperature (77^{o}K). However AC loss is a problem. A major component of AC loss is coupling loss in multifilamentary tapes. Because of varying magnetic field, the current is pushed out of superconducting filaments into the silver matrix. This effectively couples the filaments resulting in increased AC loss. Thus, the technical challenge is to fabricate HTS tapes that operate with negligible AC loss.

In this study the coupling loss was investigated by measuring transverse resistivity, $\rho_{\perp}$, a parameter describing a component of AC loss in HTS materials. Broad consideration is given to work conducted in the past. The project consists of two essential parts based on multifilamentary Bi-2223/Ag untwisted tapes: (1) materials processing and (2) measuring $\rho_{\perp}$ value.

Samples were produced by the conventional powder-in-tube (PIT) processing method. Monocore Bi-2223/Ag wires were drawn and restacked into a round pure Ag tube prior to further drawing and rolling without any annealing. The final wire was then drawn and rolled to different aspect ratios. The composite was heat treated in a two-step sintering process, which ensured high grain connectivity.

XRD, optical microscopy and I_c measurements were performed for the tape characterisation. It was also found out the tape has neither bridging nor discontinues.

The value of $\rho_{\perp}$ is obtained from magnetic hysteresis loops using the Campbell modified coupling loss model, and Carr's modified equation for fields parallel to the tape face. For each length of sample and different excitation field frequency, the magnetic hysteresis loop is plotted and the loss is obtained as $Q = \oint M\, dH$. The hysteresis loops were measured by the induction method.

Chapter 2

High Temperature Superconductors

Introduction

Since the superconducting materials were discovered a huge investigation involving major experimental work was started by various researchers worldwide.
This experimental work covers the influence of tape geometry and filament architecture on the AC loss in multifilamentary Bi-2223/Ag tapes. This project includes preparation and characterization of multifilamentary (MF) Ag/Bi-2223 untwisted tape.
This chapter also covers the critical state model briefly.

2.1 Superconductivity

Superconductors are materials that have practically zero electric resistance below the critical temperature T_c; that is why they are called 'Superconductors'. The superconducting state is a thermodynamic phase of the material. The superconducting phase can only exist at magnetic fields weaker than the critical magnetic field H_c. Mainly there are two types of superconductors. Type I superconductors are the elements of periodic table with single H_c. Type II are alloys made from elements, having two H_c. Magnetic fields weaker than H_{c1} (lower critical field) are completely excluded from the material by superconducting screening currents flowing in a very thin layer at the surface. Magnetic fields between H_{c1} and H_{c2} (upper critical field) penetrate the material in the form of 'flux lines',

There are two major properties of materials, the so-called "electric and magnetic" properties, which categorize them as superconductors. The most important electric property of superconductors is that they can carry high current densities with very little dissipation of energy. The most important magnetic property of superconductors is that they exclude external magnetic fields and prevent field penetration in their interior.

The BCS theory was the first that could explain superconductivity in materials. BCS theory introduced Cooper Pairs to define superconducting properties, but it still can not explain some aspects of high temperature superconductors. Superconductivity occurs only at low temperatures, usually below about -170^{o}C.

Working at temperatures below 20K requires sophisticated and expensive cooling technology, which is a major drawback for large-scale use of low-temperature superconductors. Devices based on low temperature superconductors are usually cooled

with liquid Helium, which boils at a temperature of 4.2 K. This problem was largely overcome by discovery of the new high temperature superconductors with T_c>77K, the boiling point of liquid Nitrogen.

At the moment the highest known critical temperature is 133 K which was achieved for (Hg,Pb)$Ba_2Ca_2Cu_3O_x$ [1]. The most commonly used HTS materials are Bi-2212, Bi-2223 (BSSCO) and Y-123.

2.2 Ceramic Superconductors

After Bednorz and Müller [2, 3] discovered $(La_{1-x}Ba_x)CuO_4$ in 1986, many other copper oxides were found to be superconducting [4, 5]. However, only three materials have received substantial, sustained attention, arising from the hope that they could become the basis for practical high-temperature superconductors, Bi-2212, Bi-2223 and Y-123, which are briefly described below.

2.2.1 Bi-2212

$Bi_2Sr_2CaCu_2O_x$ is usually referred to as Bi-2212. Its critical temperature is approximately 80K and thus its practical application would entail operating temperatures below the boiling point of liquid Nitrogen (77 K).

Indeed it has been used in a prototype cable cooled by liquid Neon and in some prototype transformer coils that were meant to operate in the region 20–30 K. Others have considered using Bi-2212 at liquid Helium temperatures because of its better performance in high magnetic fields than LTS.

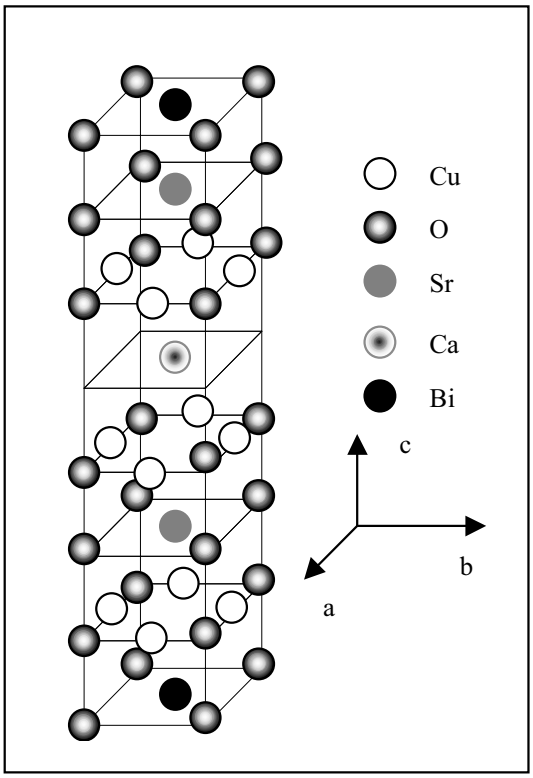

Figure 2.1 Unit cell of Bi-2212

Potential applications of Bi-2212 include NMR, high-energy physics, and fusion magnets. The appeal of Bi-2212 is that it is less expensive to fabricate than Bi-2223 and Y-123. Like Bi-2223, Bi-2212 is made in forms of long conducting wires and tapes.

2.2.2 Bi-2223

$(Bi,Pb)_2Sr_2Ca_2Cu_3O_x$ which is known as Bi-2223, is one of the three "practical" HTS materials.

Bi-2223 has the highest transition temperature of the three, approximately 106K. Thus, hope and substantial effort have been focused upon developing a conductor that would be practical at the boiling point of liquid Nitrogen. Potential applications include transformer coils and fault-current-limiter coils, as well as cable.

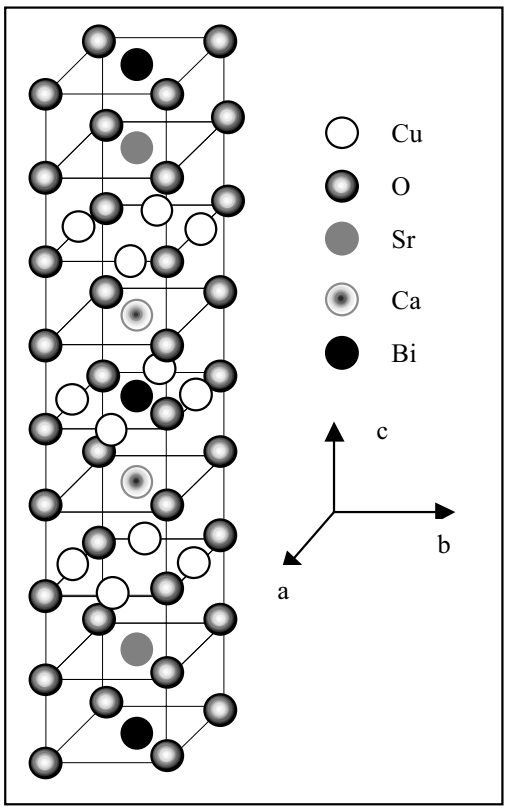

Figure 2.2 Unit cell of Bi-2223

Bi-2223 is made into a conductor by the PIT method. Unfortunately, the heat treatment is time consuming and requires excellent temperature control, which results in slower and more capital-intensive process of production than the process for Bi-2212.

2.2.3 Y-123

The third material is $YBa_2Cu_3O_x$, referred to as Y-123. It offers much better performance in magnetic fields than the two Bismuth conductors described above do. With Y-123, the current density is greater, and the anisotropy in a magnetic field is smaller. Furthermore, Y-123 films on Nickel tape have achieved "performance parity" with Bi-2223 tapes.

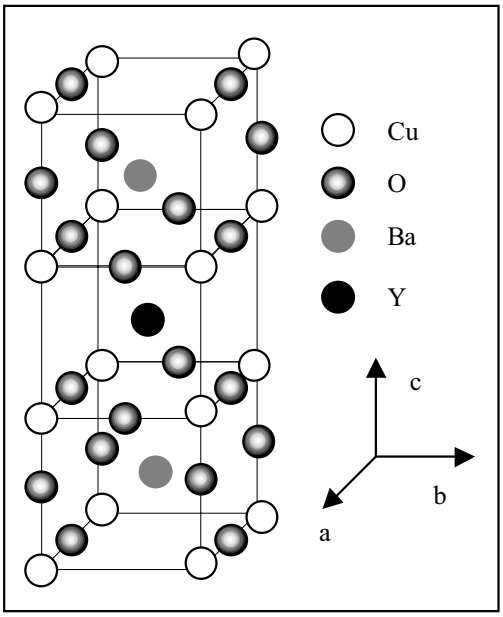

Figure 2.3 Unit cell of Y-123

In part because Nickel is much less expensive than silver, this work has raised hopes for less expensive tapes. Furthermore, since Nickel is not so good a conductor as silver, eddy currents and concomitant problems should be suppressed. However it is still not possible to make long Y-123 conductors of high enough quality.

2.2.4 Crystal Structure of HTS

The HTS are known as a mixture of metal oxides, which display the mechanical and physical properties of ceramics. A key element to the behaviour of these materials is the presence of CuO_2. CuO_2 layers are sandwiched between layers of other elements in the crystal structure of almost all HTS ceramics.

For two Bi-compounds, a single unit cell is pictured in Figure2.1 and 2.2. The **a**- and **b**-directions of the crystal are defined whitin the CuO_2-layers. The transfer of superconducting current is localised almost entirely in the CuO_2-layers. Therefore, the

ceramic materials are anisotropic. The critical-current density is higher in the **ab-**plane than in the **c**-direction. Furthermore, an external magnetic field in the **c**-direction decreases the critical-current density much more than an equally strong magnetic field in the **ab-**plane.

2.2.5 Anisotropy

High-amperage ceramic superconductors are anisotropic materials because: (1) The crystals of the superconductor are anisotropic and (2) the tape is made to preserve this anisotropy instead of randomly orienting different crystals, which would make the macroscopic sample isotropic. In practice, Bi-2223 and Bi-2212 are made in the form of tapes with large aspect ratios.

The main manufacturing goal is to align the crystals' **c**-axis parallel to each other within the tape. A further manufacturing goal is to align the **a**-axis and **b**-axis of each crystal with all the others. The critical current density is largest in the **ab-**plane of each crystal. This is the plane in which the current is intended to flow when the tape is fabricated.

Moreover, the critical current in the **ab**-plane is reduced by the presence of an external magnetic field. The amount of reduction depends very much on the orientation of the field with respect to the crystal. Fields parallel to the **ab**-plane have the least effect; fields parallel to the **c**-axis (perpendicular to the **ab-**plane) have the most detrimental effect.

2.3 Multifilamentary Ag/Bi-2223 Tape Preparation and Properties

There are several ways to classify conductor technologies. Three HTS compounds are mainly used for most large-scale power applications: Bi-2223, Bi-2212, and Y-123 (Section 2.2). Based on the Bi-2223 tapes used in this research, the relevant tape making methods are considered. The four major techniques used to manufacture HTS conductors are: (1) Powder In Tube method (PIT), (2) Dip coating and other ceramic coating methods, (3) Deposition of biaxially textured thin films on textured buffer layers or substrates and (4) Bulk growth techniques. In this study the samples were produced by the PIT method which is described in some details.

2.4 Process for Making PIT Conductors

The sheathed or powder-in-tube (PIT) process was one of the first to be developed for making HTS conductors and still is used. It is sometimes used for Bi-2212 but is almost always used for processing Bi-2223 into a conductor. Figure 2.2 shows the steps, which are followed in the process.

The material of choice for the tube is silver or a silver alloy. Silver is permeable to oxygen, is non-reactive with the HTS core material, lowers the melting point of Bi-based HTS materials during thermal processing, and forms a template upon which the HTS material can grow.

Typically, the tube is filled with HTS powder, then extruded or drawn to a wire. The powder consists of fine Bi2223 grains. For multifilament conductors, the wire is usually drawn in a hexagonal shape, cut into shorter lengths, and formed into a stack of 7, 19, 37, 55, 61, 85, or a higher number of filaments. This stack is then inserted in another

tube, and the composite is extruded or drawn to wire. The restacking and redrawing steps are omitted for monofilament wire.

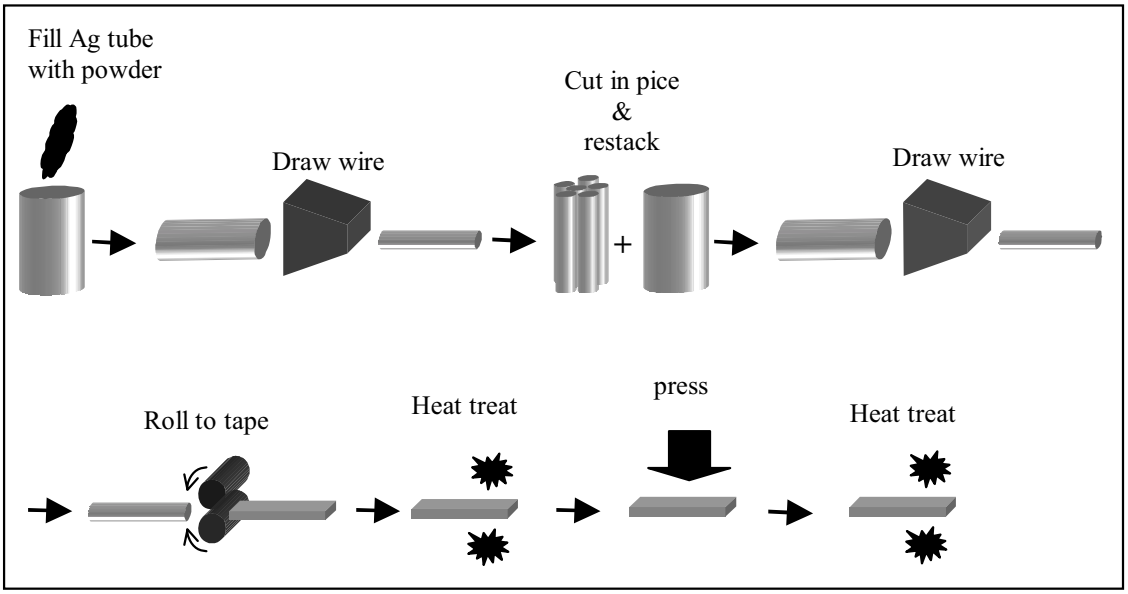

Figure 2.4 Schematic diagram of the Powder-In-Tube method for fabricating HTS tapes

For round wire, the final step is heat treatment, but Bi-2223 conductors are made in a flat "tape" format, achieved by rolling the wire to a wanted aspect ratio.

Fine filaments of Bi-2212 are subjected to a partial melt process at 800-900°C to form large grains of that compound. The grains are oriented parallel to the wide face of the tape by intermediate pressing or rolling, Bi-2223 is formed by sintering, whereby Bi-2223 grains are textured. The sintering temperature and heat treatment is carefully chosen for a particular composition of the powder and needs to be accurately controlled within 1K.

Both Bi-2223 and Bi-2212 are highly anisotropic materials, and the superconducting current is located within the **ab-** plane (CuO layers). Obtaining good uni-axial (**c**-axis)

orientation of the grains in these two materials is necessary to achieve high critical current density (J_c) [6].

2.5 Modeling HTS Materials with CSM

Modelling HTS materials can help to explain their superconducting phenomena (Section 2.1). The classical Critical State Model (CSM) introduced by Bean [7] has been successfully used to describe the J_c of type-II superconductors. The CSM model is used for the calculation of J_c from magnetic hysteresis loops of classical type-II superconductors; it provides approximate solutions for most practical cases, even for those where the critical current density depends on magnetic field.

In type-II materials a magnetic field penetrates the superconductor in the form of flux lines. Transport current causes a Lorentz force that tends to move the flux lines through the material in a direction perpendicular to the current. This motion is called flux flow and is a dissipative process. The motion of flux lines corresponds to a change in the internal magnetic field, which causes an electric field according to Faraday's law. The electric field E increases linearly with the transport-current density. The flux-flow resistivity is usually higher than the resistivity of a good normal conductor. Flux flow is therefore undesirable.

Preventing the movement of this lattice when the superconductor is carrying a current is crucial for obtaining good superconductor performance. Unlike LTS, the flux lines in a HTS are arranged in what has been called a "vortex glass" where there is no regular lattice. The anisotropy (Section 2.2.4) of a high-temperature superconductor causes the flux in a given layer to form "pancake vortices" [8, 9]; when the coupling between layers is weak compared to thermal energies, these vortices interact strongly within each CuO_2

layer but only weakly with neighbouring layers. This makes it difficult to pin the vortices, because pancakes that are free to move in one layer can move relative to pinned pancakes in adjacent layers. Indeed, bismuth compounds cannot tolerate significant magnetic fields at 77 K because the vortex glass lattice has "melted," leaving the pancake vortices relatively free to move. Thus, the better the vortex coupling between adjacent copper oxide layers the better the performance of the superconductor.

In the critical state model the superconducting current density is assumed to be the critical current density ($J=J_c$) [7]. When applying an external field, that field starts to penetrate at the boundary of the superconductor. The penetration depth depends on value of the external field and J_c [7]. Without vortex pinning, $J_c=0$ and any external field fully penetrates the superconductor in the form of moving vortices. With vortex pinning a gradient of vortex density is maintained by the pinning. This gradient defines J_c (Figure **2.5**)

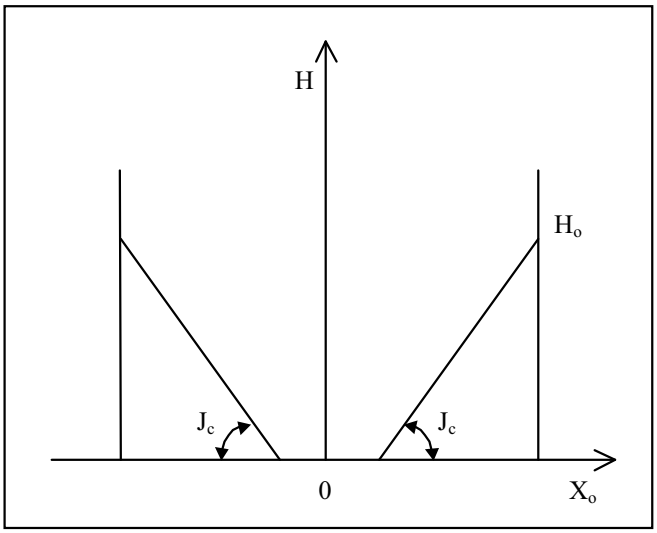

Figure 2.5 Field profiles in a superconductor according to the CSM model. X_o is the edge of the sample and H_o is the value of external field.

The Magnetisation of a tape is obtained from the integral of the critical current density over the volume of superconductor occupied by the field. Critical current density can be calculated from measured magnetic hysteresis loops using the critical state model [7]: $J_c = k\Delta M / D$, where k is a constant, ΔM is the height of the hysteresis loop, and D is the thickness that the sample presents to the applied field.

The basic assumption of the CSM is that in the regions where the local current density J is less than the critical one J_c, the flux lines do not move. This assumption does not hold for any finite temperature because of thermally activated flux motion or flux creep [10]. Basically, flux creep is the phenomenon which causes resistance is superconductors. Flux creep in metallic Type II superconductors is very small and the decay constant for the current in such superconductors is too long. This allows them to be used to generate large, stable magnetic fields. In HTS materials this field is much higher, but it decays because of weak vortex pinning and strong thermal excitation.

Chapter 3

AC Loss

Introduction

This chapter will be devoted to a brief review of the past work conducted in the field of present study. It should be mentioned that due to the existence of an enormous number of reports, the review will be focused solely on the literature that has a direct relevance to the present work.

This chapter describes AC loss in HTS. A brief reference is given to explain the types of AC loss in superconducting materials. A short description of different AC loss models are presented, which is used in our experiment.

3.1 AC Loss in Superconductors

Alternating magnetic fields and transport currents cause dissipation of energy in HTS materials. The energy dissipation is called the AC loss.

AC losses are generated by three mechanisms: (a) hysteresis in the superconductor; (b) ohmic loss in the metal matrix when current flows from one superconducting filament to another, often called coupling loss; and (c) ohmic loss in the metal sheath enveloping the filaments, that is generated by induced eddy currents, which flow even when there is no transport current in the superconducting filaments.

The theory of AC losses in multifilamentary LTS wires is well described by Wilson [11] and Carr [12]. Recent results on AC losses in multifilamentary Bi-2223 show that this theory is applicable to high -T_c tape as well, with some modifications [13, 14]. Most of the same fundamentals of AC loss discovered for LTS apply to HTS as well. However, there are some differences, which can be grouped into three areas. The first of these is an intrinsic property of HTS superconductors, namely the higher level of magnetic relaxation in these materials. The second two are (a) outer strand geometry and demagnetisation, and (b) the filamentary array configuration within the strand. These latter two items are of course not intrinsic properties of HTS, but they are more or less regularly associated with them in practice [15].

There are different type of AC loss that could occurred in a supercoduting tape namely: the Hysteresis Loss, the Eddy Current Loss and the Coupling Loss.

3.1.1 Hysteresis Loss

Hysteresis losses are a result of irreversibility caused by vortex pinning. They are called hysteresis losses because the flux that has entered the superconductor does not leave

precisely in the same manner by which it entered due to the pinning. If one plots the magnetic induction, *B*, versus the magnetic field, *H*, a hysteresis loop is obtained, which is traversed once per cycle. The energy loss per cycle is proportional to the area of this loop, provided that no transport currents are flowing. Such hysteresis losses are dissipated as heat.

According to the CSM model, the current density in a superconductor is equal to the critical current density. If a superconductor is carrying an AC current, the current distribution at the peak AC current is the same as it would be for the same value of DC current. The thickness of this current-carrying sheath varies during an AC cycle. (This is true for both transport and shielding currents.) When the transport current or external field producing the shielding currents is large enough, the current sheath reaches the centre of the superconductor. This is called "full penetration." Losses differ below and above full penetration, and depend on the direction of the applied fields.

There are two strategies for reducing hysteresis losses in multifilamentary composites: increasing the critical current density and decreasing the filament diameter.

3.1.1.1 Increasing Critical Current Density

A number of approaches are available for increasing the critical current in BSSCO. Perhaps the two most important are (1) increasing the strength of weakly linked areas of the superconducting material and (2) improving the vortex pinning.

The first of these approaches involves changes in processing techniques to achieve phase purity and better *c*-axis alignment, while the second introduces defects in the superconductive crystals.

Increases in critical current density have been achieved by optimising the homogeneity of the precursor powders used in the conventional Powder-In-Tube (PIT) method of

fabricating BSCCO wires. As the Bi-2212 phase is converted to the Bi-2223 phase, the degree of texturing (the area occupied by a given phase) of the Bi-2212 phase is transferred to the Bi-2223 phase. The goal is to maximise the Bi-2223 phase by optimising the processing.

3.1.1.2 Decreasing Filament Diameter

Where the field is greater than required for full penetration of field into the superconductor, the hysteresis loss is proportional to the thickness of the superconductor perpendicular to the field (section 3.2.1). This proportionality provides the incentive for reducing the diameter of the superconductor and, to obtain adequate current-carrying capacity, for making multifilament wires. With superconducting tape, it is the thickness of the superconductor in the direction perpendicular to the tape surface that is important. In tape where the filaments are untwisted, the coupling currents can become large enough to saturate the filaments. At that point, the multifilamentary core behaves as one large filament with large hysteresis losses. Therefore, for the strategy of employing multiple filaments to be effective, it is important that full coupling be avoided.

3.1.2 Eddy Current Loss

It is clear from the text that when an external time-varying magnetic field penetrates into a normal conductor, it induces a changing electric field, which in turn causes currents to flow. These are known as eddy currents.

Due to eddy currents in the normal-conducting sheath around the tape, the ohmic energy dissipation can be significant if the magnetic field is perpendicular to the tape. At low frequencies the eddy-current loss can be calculated for many conductor geometries [16].

The basic approach to reducing the eddy current losses is increasing the effective resistivity of the matrix. The eddy current loss is negligible in our research.

3.1.3 Coupling Loss

An eddy current induced by a varying magnetic field, flows partly through the superconductor and also through the silver between the filaments. When currents flow from one filament to another, the currents couple the filaments together into a single large magnetic system, and is encountered with a resistance along the currents path through the silver matrix. This ohmic loss in the metal matrix is often called the coupling loss.

3.2 AC Loss Measurement in Multifilamentary Tapes

Different types of AC loss occur in HTS multifilamentary tapes. Measurements of the occurred loss in a multifilamentery tape are needed to obtain relations between AC loss parameters. AC loss depends on a number of parameters. One is the direction of the exposed magnetic field, i.e. perpendicular or parallel to the tape face. Another one is the tape shape; always tapes are fabricated in various shapes, which may either be twisted or untwisted. The shape factor (n) and the tape length (L) are considered in tape fabrication.

Later in 1977 K.Kwasnitza [17] introduced the Scaling Law to ease the AC loss measurement. The law was built on frequency dependence of the overall AC loss. He showed that the losses are a unique function of $\omega\tau$ at constant amplitude (ω is the angular frequency and τ a characteristic time constant). He carried out his experiments on twisted samples of NbTi multifilametary Cu sheeted tape exposed to perpendicular magnetic field.

In 1982 A.M.Campbell [18] extended K.Kwasnitza's early work on Scaling Law [17] to different amplitudes and tape shapes in low frequency ($\omega\tau$<<1). He calculated the coupling current loss per unit volume per cycle for twisted samples, which reads as:

$$Q_c = \frac{n\pi B_0^2 \omega\tau}{\mu_0(1+\omega^2\tau^2)} \quad \text{Jm}^{-3} \qquad \text{Eq 3.1}$$

where n is the shape factor, B_0 is the applied external field, ω is the angular frequency and τ is the time constant. The diamagnetism of the filaments limits Eq 3.1 to the coupling loss per volume per cycle as:

$$Q_c = n\pi\mu_{eff}\mu_0 H_0^2 \frac{\omega\tau}{1+\omega^2\tau^2} \quad \text{J cycle}^{-1}\ \text{m}^{-3} \qquad \text{Eq 3.2}$$

In Eq 3.2 μ_{eff} is defined so that B in the system is given by $B = \mu_{eff}\mu_0 H_a$, where H_a is the field due to the external magnet and surface filament current and μ_0 is permeability of vacuum. Eq 3.2 can be reduced to:

$$Q_c = n\pi\mu_0 H_m^2 \omega\tau \qquad \text{Eq 3.3}$$

which was proposed by Campbell in SI unit. In Eq 3.3 H_m is the applied field amplitude. This relation applies in the condition of low frequency ($\omega\tau$<<*1*) prevails.

Campbell [18] described that the coupling loss in higher frequencies and amplitudes could be predicted from the coupling loss in the low frequencies and amplitudes. He also predicted [18] the loss diagram as a function of frequency which is shown in Figure 3.1. The diagram applies when the amplitude is less than the full penetration field.

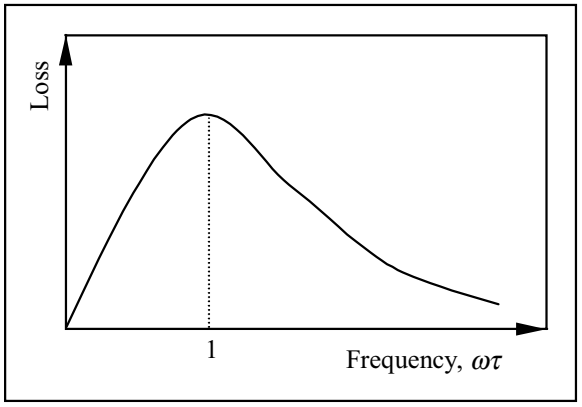

Figure 3.1 Frequency dependence of coupling current loss, with amplitude of external field smaller than the field of full penetration [18].

Figure 3.1 is a Gausssian function which is given by Eq 3.2 for the coupling loss, only if the field including the demagnetizing effects is less than that required to fully penetrate the conductor [18].

Campbell also calculated the loss for different strand shapes. He defined the time constant, τ, for each shape and its properties, which are listed below in SI system of units [18].

i) Round strands. The shape factor is n=2 and $\tau=\mu_0(1/8\pi^2)L_p^2/\rho_\perp$

ii) Rectangular strands whit $a>>b$ and field parallel to b. The shape factor is a/b and $\tau=\mu_0(7/480)(a/b)L_p^2/\rho_\perp$

iii) Rectangular strands whit $a<<b$ and field parallel to b. The shape factor is a/b and $\tau=\mu_0(1/16)(a/b)^2L_p^2/\rho_\perp$

In the above relations $\rho_\perp$ is the effective transverse resistivity, L_p is the pitch length of the tape, a is the thickness and b is the width.

According to his calculation for round twisted tape, the shape factor n=2 and the relaxation time τ in S.I. system is:

$$\tau = \frac{\mu_0 L_p^2}{8\pi^2 \rho_\perp} = \left(\frac{1}{2\pi}\right)\frac{L_p^2}{10^9 \rho_\perp} \qquad \textbf{Eq 3.4}$$

Campbell's modified Eq 3.3 and Eq 3.4 in c.g.s. system, are expressed respectively as[21]:

$$Q_c = n\left(\frac{1}{4}\right)H_m^2 f \frac{L_p^2}{10^9 \rho_\perp} \qquad \textbf{Eq 3.5}$$

$$Q_c = n\left(\frac{\pi}{2}\right)H_m^2 f\tau \qquad \textbf{Eq 3.6}$$

Eq 3.5 and Eq 3.6 will lead to:

$$\tau = \left(\frac{1}{2\pi}\right)\frac{L_p^2}{10^9 \rho_\perp} \qquad \textbf{Eq 3.7}$$

Carr's [12] expression for AC loss in twisted multifilamentary tapes is well known. Tacking n=2 Eq 3.6 and Eq 3.7 show that Carr's expression [19] is in good agreement for AC loss in round twisted multifilament tape. In other words Campbell and Carr ideas for round twisted tape support each other.

In 1994 Kwanitza and Clerc [20] reviewed Campbell's relations for different strands shape. They carried out their experiments on Bi2223/Ag untwisted tape exposed to field parallel to the tape face (width b). Their experimental results satisfied Campbell's relation for round twisted tape (Eq 3.6, Eq 3.7) with insertion of a prefactor 0.81 and replacement of L_p by $2L$ [13]. These two values are the same values that converts Carr's basic expression for round untwisted strands to Campbell's equations [21]. Rewriting Eq 3.7 with these two values gives $\rho_\perp$ as [22, 23]:

$$Q_c = \frac{0.81}{4} n \frac{L^2}{10^9 \rho_\perp} H_m (dH/dt) \qquad \textbf{Eq 3.8}$$

$$\rho_{\perp} = \left(\frac{1}{2\pi\tau}\right)\frac{4L^2}{10^9}$$

Eq 3.9

$$\rho_{\perp} = (4/10^9)L^2 f_c$$

Also the relations obey Kwasbutza's [17] Scaling Law, depending only on the reduced frequency $\omega\tau$. It is examined [21] that for untwisted tapes, Eq 3.8 remains unchanged and an independent τ from shape factor $n=a/b$ can be obtained (Eq 3.9), which is an extended relation of Campbell's relation for round strands.

In order to calculate the coupling loss, Q_c, Kwanitza and Clerc [13] assumed a sinusoidal field ΔB parallel to the tape face (width b) and achieved the following relation.

$$\frac{Q_c}{V} = \frac{1}{2\mu_0} n\Delta B^2 F(u) \qquad \textbf{Eq 3.10}$$

Where V is the matrix volume and $F(u)$ is the loss parameter. Tacking $u=\pi\sqrt{(\omega\tau/2)}$ the function $F(u)$ is expressed as:

$$F(u) = \frac{1}{u}\left(\frac{\sinh u - \sin u}{\cosh u + \cos u}\right) \qquad \textbf{Eq 3.11}$$

The illustration of loss parameter, F, as a function of $\omega\tau$ gives a similar diagram as shown in Figure 3.1, which comes to its maximum at $\omega\tau$=1. Eq 3.10 was obtained using a diffusion-flux model, which is compatible with the pervious obtained Eq 3.1 for fixed coupling loss[13]. They also have reported that the eddy-current losses could occur in Ag matrix of tapes in the absence of the superconducting filaments, which is negligible for $f \leq 50$Hz in comparison to the coupling losses[13]. This is due to the large $\rho_{\perp}$ compared to the matrix resistivity, ρ_{Ag}. Collings, et al [24] have examined this phenomena using Block-Grüneisen theory [25]. They understood that the unexpected large $\rho_{\perp}$ compared to ρ_{Ag} is due to the influence of flux creep on the superconducting portion of the eddy current

paths at relatively high temperatures and/or high magnetic field. They showed that this phenomenon is not completely compatible with Block-Grüneisen theory and could be explained by a simpler model.

Chapter 4

Experimental Layout and Methodology

Introduction

This chapter explains the procedure by which the experiments are conducted. The procedure describes all the steps covering the selection of the materials and the AC loss measurements. The powder used to make the tape, method of tape making, instruments and methods of measurement are also explained.

4.1 Preparation of the Tapes

For all samples, 200gr of Bi-2212 powder was used. The powder is produced by Merck Inc & Co. and provided by Australian Superconductor. This company is a HTS tape manufacturer and large consumer of Bi-2212 powder. Usually the powder composition is tested before making the tape and this test was initially done by Australian Superconductor.

Following the PIT method (section 2.4), 16gr Bi-2212 powder was packed in a 20cm length of pure silver tube of 12mm outer diameter and 1.25mm wall-thickness. The inner wall was brushed until it shone and sealed on one end. Sealing the end of the tube with spiral Bi-2223/Ag tape results in a capsule containing the Bi-2212 powder.

After degassing the capsule at 600^{o}C for 10hr, it was drawn to produce 2.31mm diameter wire without any annealing. Eight pieces of 24cm length wires were restacked in a pure silver tube with brushed shiny inner wall, 20cm in length, outer diameter of 10mm, and wall thickness of 0.8mm. Eight of the pieces were cut longer than the length of the restacking tube to produce a symmetrical alignment in the tube as shown in Figure 4.1.

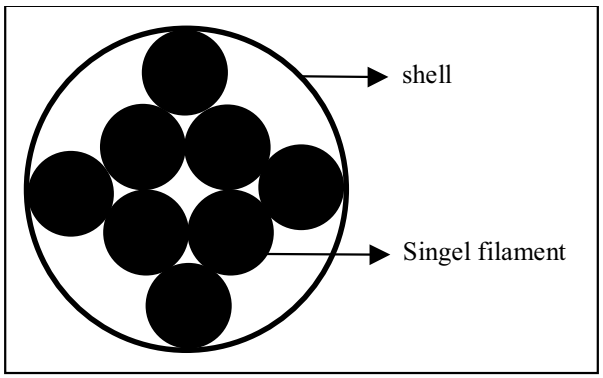

Figure 4.1 The configuration of the filaments in the restacking tubes

The restacked tube was then drawn without annealing to produce a wire of 1.5mm diameter, after degassing at 600°C for 10hr. The wire was then rolled to produce tapes with aspect ratios of 1/2, 1/5, 1/10, with no annealing.

To prevent any sausaging phenomena [26], the tape was drawn and rolled without annealing at room temperature. This procedure however, introduces cracks and breaking along the wire, which becomes a major problem in the rolling stage but not as serious as the sausaging phenomena during the heat-treatment.

To obtain the best sintering temperature the heat treatment was varied for different samples taken from the tape. During these experiments, just one oven was used in which the accuracy of temperature control was $\pm 1^{o}$C.

The optimal sintering temperature varies depending on different factors, among them the sheath wall thickness, which is considered in this research.

After XRD and I_c examinations on the samples, the optimal heat treatment procedure was obtained as shown in Figures 4.2 and 4.3.

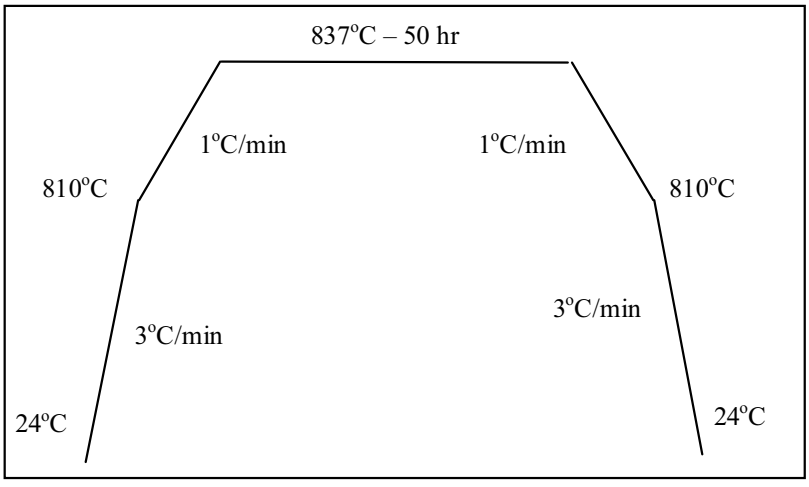

Figure 4.2 Schematic diagram for the first step of heat-treatment for the 8-filament tape

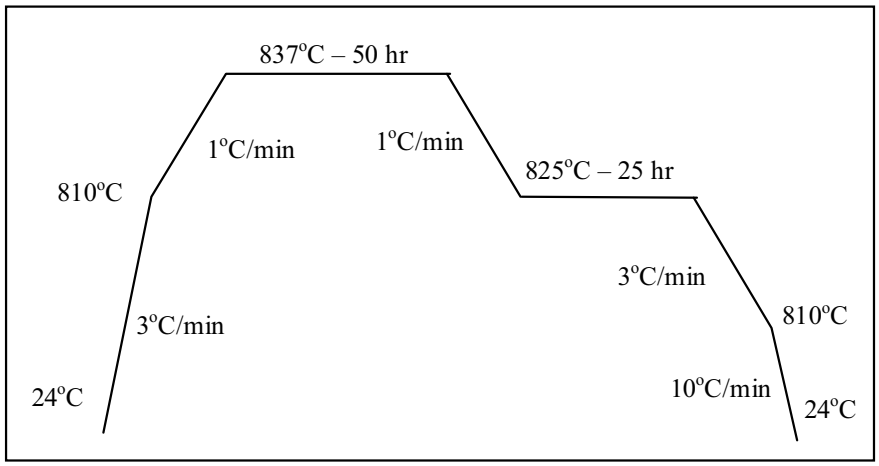

Figure 4.3 Schematic diagram for the secound step of heat-treatment for the 8-filament tape and after pressing

The tapes were pressed between the two sintering stages, with 5%-10% reduction in thickness.

4.2 Characteristics of the Obtained Tapes

In this step of the experiment, I_c measurement, XRD and optical microscope examination were used to characterise the tapes.

4.2.1 XRD

The fabricated tapes under the XRD test are identical to Figure 4.4, which shows a small amount of Bi-2212 after the second sintering. The relevant reflected peak for Bi-2223 and Bi-2212 are indexed.

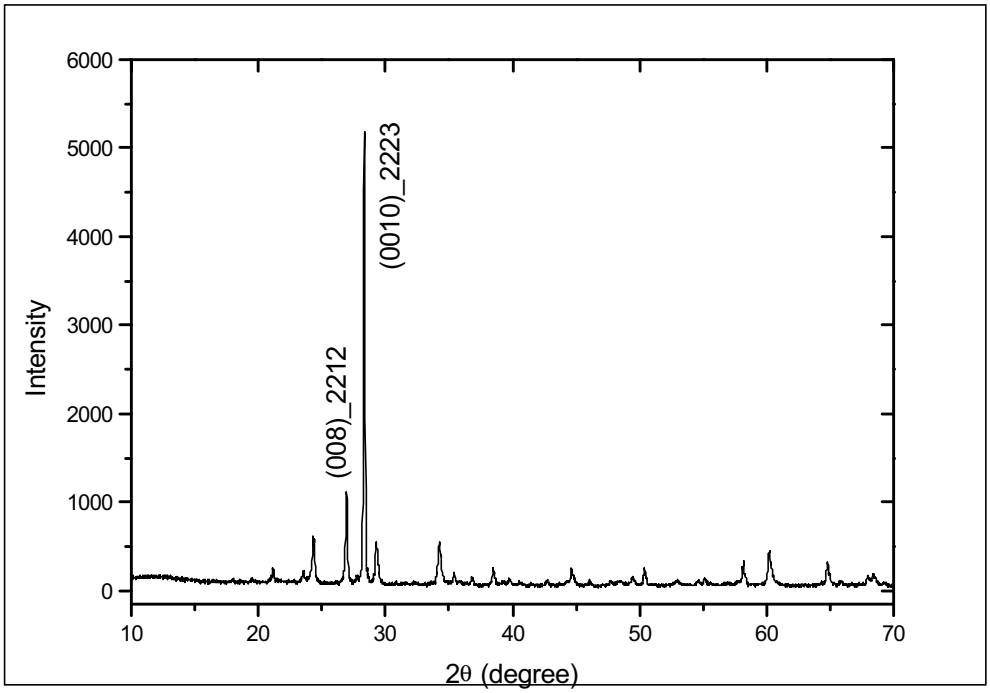

Figure 4.4 XRD for 8 filament tape after second sintering

The peak points are identified from the ICDD database and are shown in Figure 4.4 The percentage of Bi-2223 phase in the phase mixture, $X_{Bi\text{-}2223}$, was defined by the equation[27]:

$$X_{Bi2223} = \frac{I_{Bi2223}^{(0010)}}{0.88 I_{Bi2212}^{(008)} + I_{Bi2223}^{(0010)}} \qquad \textbf{Eq 4.1}$$

where $I_{Bi2223}^{(0010)}$ and $I_{Bi2212}^{(008)}$ are the integrated intensities of X-ray diffraction *(0010)* of Bi-2223 phase and *(008)* of Bi-2212 phase. The results obtained from the XRD show there is about ~87% Bi-2223 phase formed after the heat treatment of the tapes.

4.2.2 Critical Current of the Tape

The measured I_c for the tapes is summarized and is shown in Table 4.1.

Table 4.1 The I_c for different thickness of the 8-filament tape

Thickness (mm)	0.18	0.24	0.33
I_c (A)	11.20	17.85	13.80

The table shows the electrical properties of the tapes after sintering. Plotting I_c vs. thickness (Figure 4.5) shows that the optimum thickness could be somewhere around 0.25mm. The thinner the tape is rolled, the more cracks are introduced, and the thicker the tape is rolled the worse the alignment of the grains.

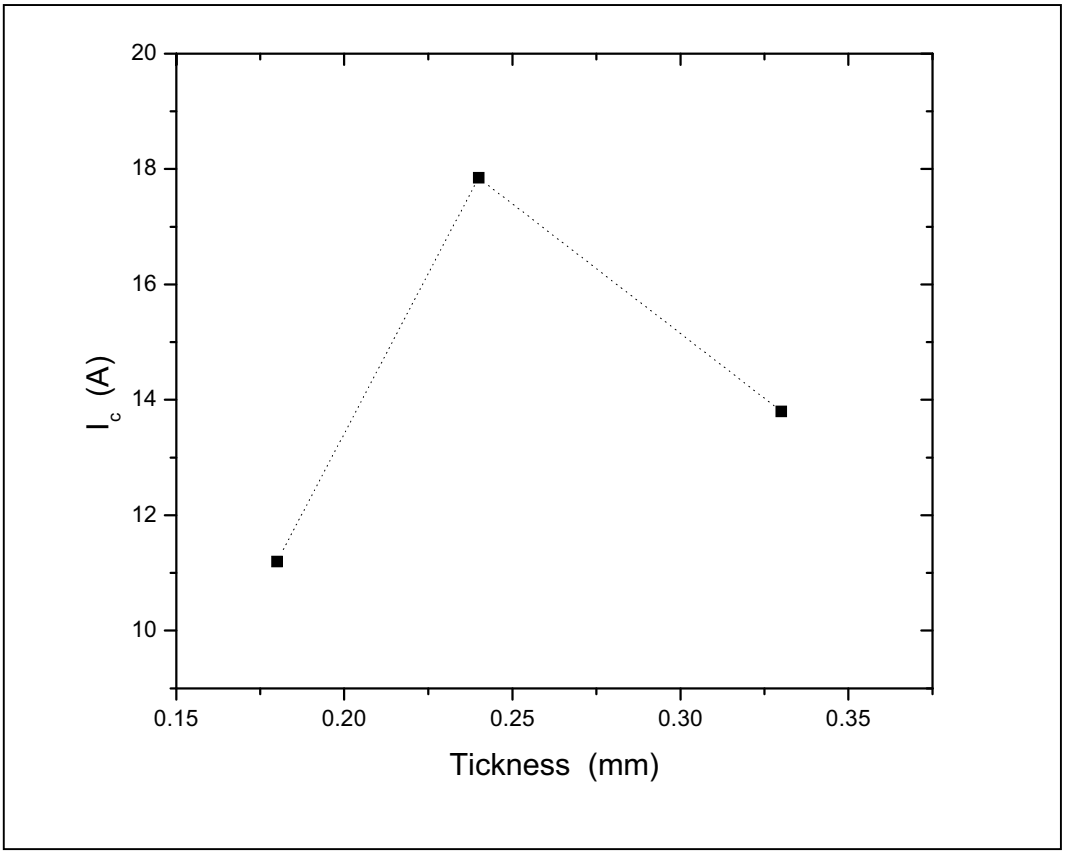

Figure 4.5 I_c vs. Thickness of 8 filament tapes

4.2.3 Microscopic Examination of the Tapes

The optical microscope pictures of the tapes are shown in this section. The picture indicates no bridging between the filaments inside the tape, and that the superconducting filaments are not discontinuous. This is because of the large wall thickness of silver between the filaments and also due to the drawing and rolling of the filaments. The restacking of the wires without annealing also contributes to this.

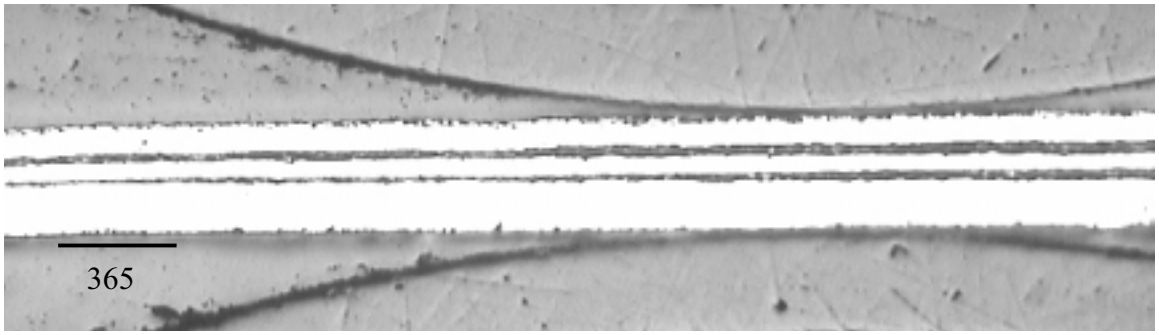

Figure 4.6 Microscopic image of the 8-filament tape in the direction parallel to the length of the tape

4.2.3.1 Microscope Images of Cross Sections of 0.18mm Thick Tapes

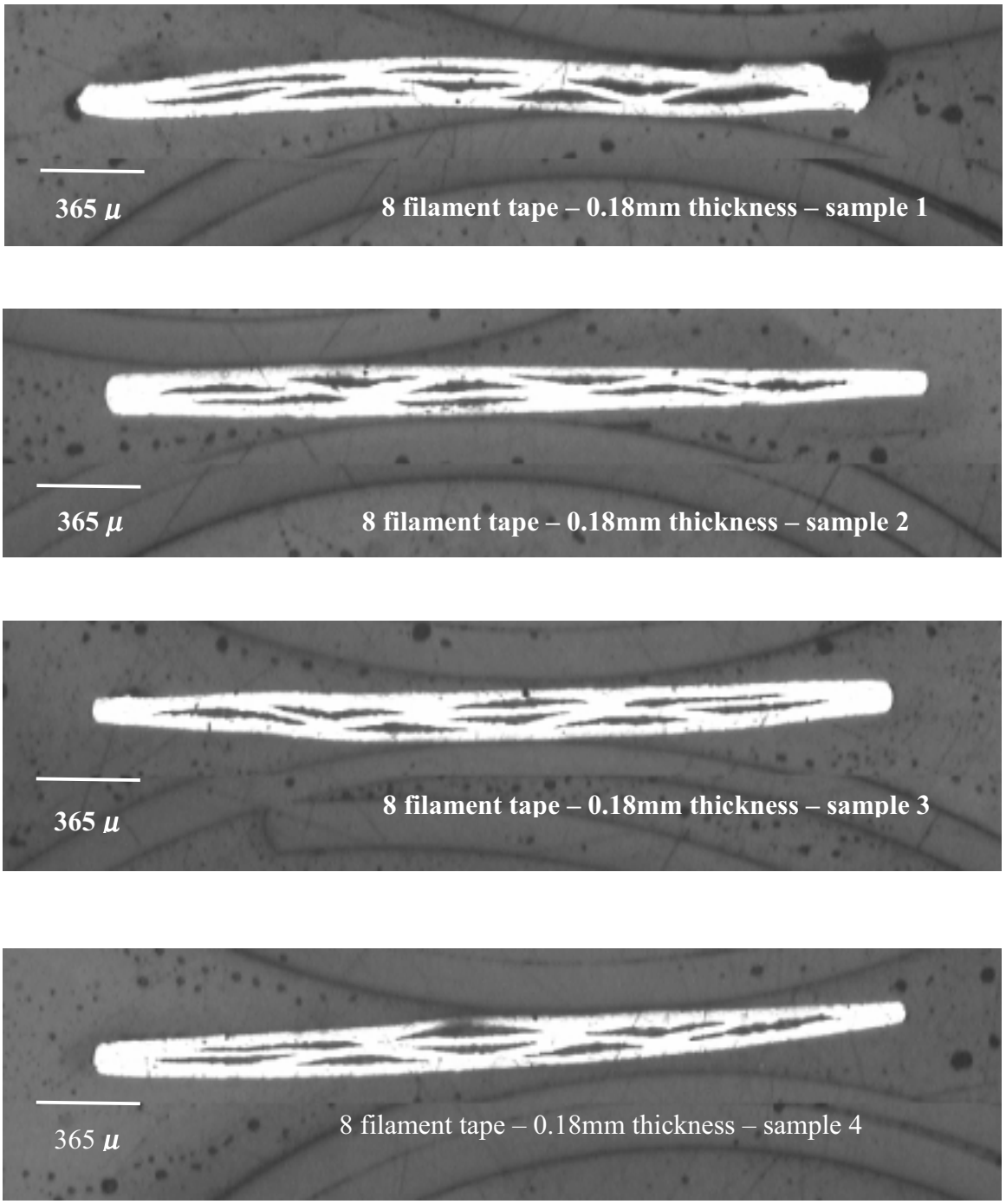

Figure 4.7 Microscopic images of 4 cross-sections of 0.18mm thick tape

4.2.3.2 Microscope Images of Cross Sections of 0.24mm Thick Tapes

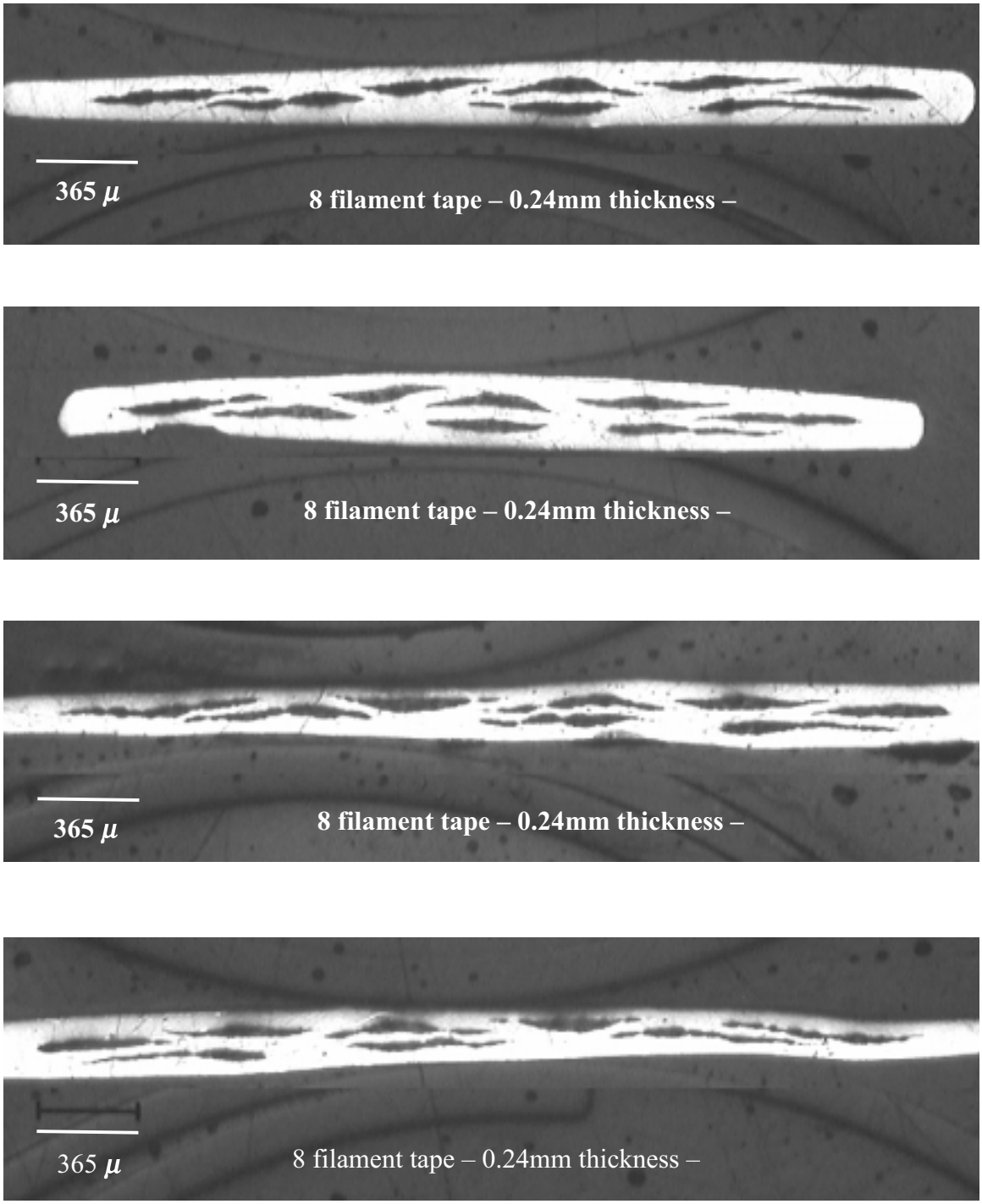

Figure 4.8 Microscopic images of 4 cross-sections of 0.24mm thick tape

4.2.3.3 Microscope Images of Cross Sections of 0.33mm Thick Tapes

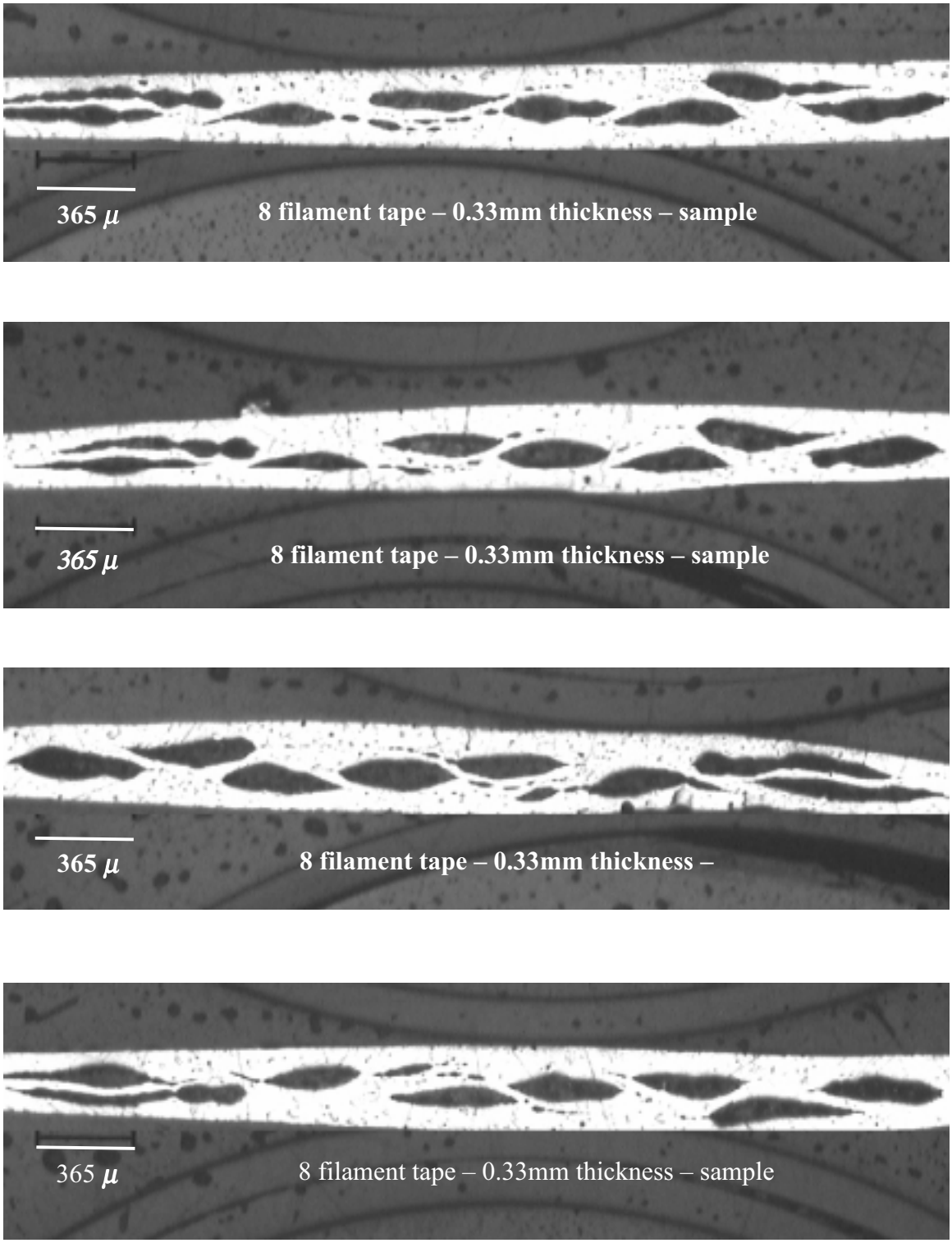

Figure 4.9 Microscopic images of 4 cross-sections of 0.33mm thick tape

4.3 AC Loss Measurement Device

In this study the pickup-coil method was utilised for measuring the AC loss. The apparatus was designed at ISEM. A schematic layout of this type of AC loss measurement device is demonstrated in Figure 4.10.

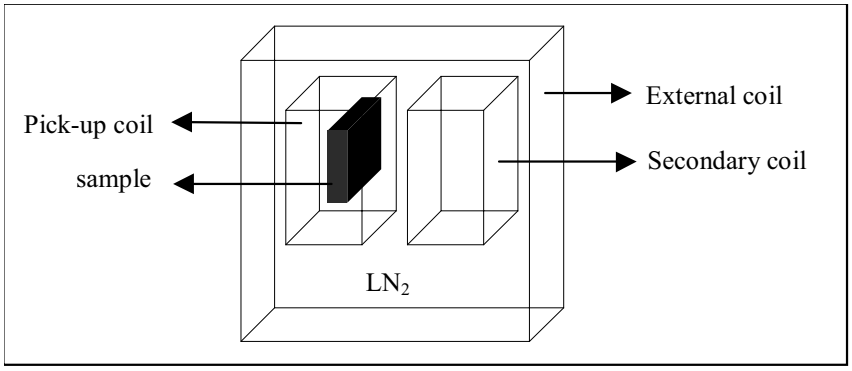

Figure 4.10 Schematic diagram of AC loss measurement device

As shown in Figure 4.10, two parallel pick-up coils are placed in a solenoid coil. The solenoid is driven by an AC current source Pacific Power 3120AMX and produces an AC magnetic field. Without a sample in the system, the signals of the two pick-up coils are zeroed. When a sample is placed in one of the coils, the net signal is proportional to *dM/dt*. The electronic parts of the measurement device are schematically shown in Figure 4.11.

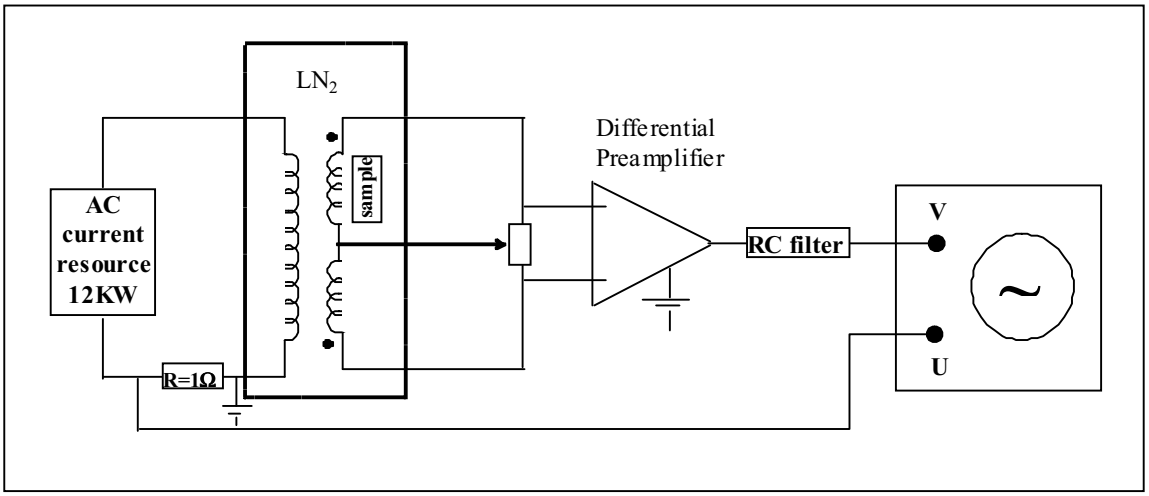

Figure 4.11 Schematic diagram of electronic parts of the AC Loss measurement device used in the study

The signal from the pick-up coils is $V = -\frac{d\phi}{dt}$ **Eq 4.2**

where ϕ is the magnetic flux in the coils $\phi = A_1(H + m) - kA_2H$ **Eq 4.3**

A_1 is the average surface area of the coil containing the sample and A_2 of the compensating coil and m is magnetic moment of the sample. *k* is an adjustment factor that ensures $\phi = 0$ when there is no sample in the either coil, which is adjustable by the potentiometer (Figure 4.8). For a properly compensated coil $\phi = A_1 m$ **Eq 4.4**

Therefore: $V = -A_1 \frac{dm}{dt}$ **Eq 4.5**

Form here: $m = -\frac{1}{A_1}\int V dt$ **Eq 4.6**

Therefore, numerical integration of the signal from the compensated coils gives the magnetic moment *m*. Magnetisation is *M=m/v*, where *v* is the volume of the sample.

The AC field produced by the solenoid was obtained from the voltage drop across the resistor connected in series to the solenoid, U (Figure 4.11). The field of the solenoid was calibrated with a Hall Probe:

$$H = 5.5\times10^{-3}\frac{T}{A}\cdot I \qquad \textbf{Eq 4.7}$$

where I is the current through the solenoid and resistor. I was obtained as $I=U/R$, where U is the voltage drop across the resistor. Note that $R=1\Omega$.

Plotting the obtained magnetisation M vs. field (H) (Figure 4.12), a magnetic hysteresis loop was obtained.

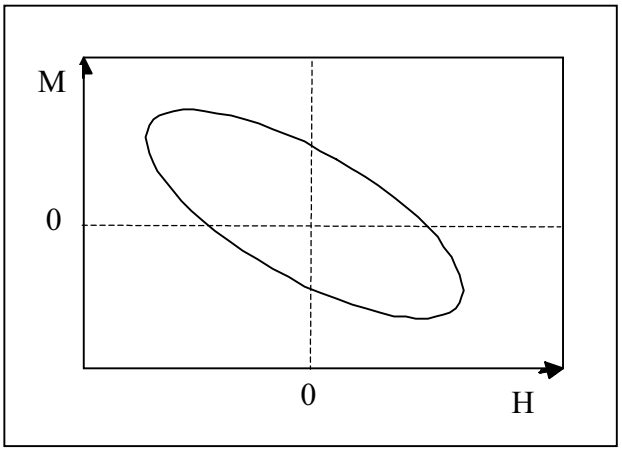

Figure 4.12 Schematic diagram of Magnetisation M vs. field H obtained

The surface area of the loop corresponds to the total loss for one cycle of magnetic field:

$$Q_{tot} = \oint MdH$$

Measurements of loss vs. frequency (Q-f) will give a peak (Figure 4.13) which corresponds to the condition $\omega\tau=1$ in the Campbell equation for coupling losses (Eq 3.9).

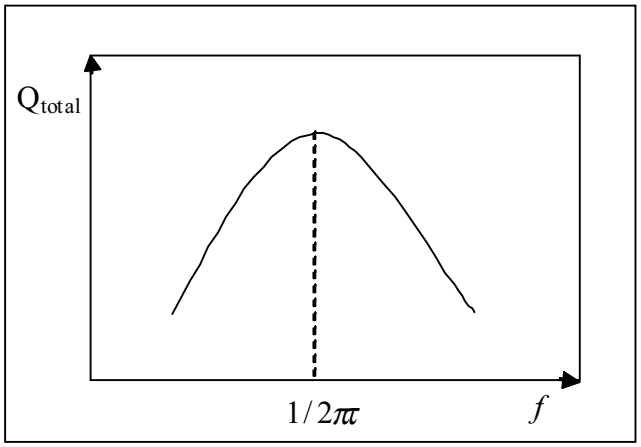

Figure 4.13 Schematic diagram of the total loss Q_{total} vs. frequency f

There are other types of losses included in Q_{total}, however they are not relevant in our analysis, because we only need to know the frequency of the maximum, which will give us the value of τ. Knowing τ, the value of $\rho_{\perp}$ can be calculated from Eq 3.9.

The data collected from the AC loss measurement device was transferred to the computer through a GPIB card programmed with LabView. The optimum filtering range was found empirically. Usually the cut-off frequency of the low-pass filter was at least 1000 times the frequency of the AC field, in order to avoid distortion of the measured signal by RC filters. The gain of the differential preamplifier was typically 1000. We used a Pacific Power 3120AMX AC source, a Stanford Research Systems SR560 differential preamplifier, and a digital oscilloscope Tektronix TDS320.

In this study, for each length of the sample, the frequency ranged from 10Hz to 250Hz in steps of 1-5 Hz. For each frequency 2-3 measurements were performed.

The area of the hysteresis loop was obtained numerically, giving the value of Q_{total}, up to the calibration factor. Since we only need the frequency of the peak in Q_{total} vs. f, there was no need to calibrate Q_{total}.

Chapter 5

Experimental Results and Analysis

Introduction

Experimental results are presented in this chapter. $\rho_{\perp}$ *was calculated and compared with the measurements reported in the literature.*

5.1 AC Loss

As described earlier, an 8 filament tape with three different thicknesses (0.18mm, 0.24mm, and 0.33mm) was studied. Samples of each of the three thicknesses were cut to three different lengths. For all the tapes the loss vs. frequency (*Q-f*) diagram was plotted. The peak point of the plot Q_{total}-f gives τ which from $\rho_{\perp}$ could be calculated.

In the following three sections, the Q_{total}-f diagram for each sample cut from the tape is presented whit its thickness. For each sample the Q_{total}-f diagram was compared with the Campbell Coupling Current Loss model, and the τ value was obtained.

5.1.1 0.18mm Thickness

The 0.18mm thickness tape was cut to three lengths of 20mm, 24mm, and 28mm. For each length the Q_{total}-f diagram is plotted (Figures 5.1, 5.2, 5.3).

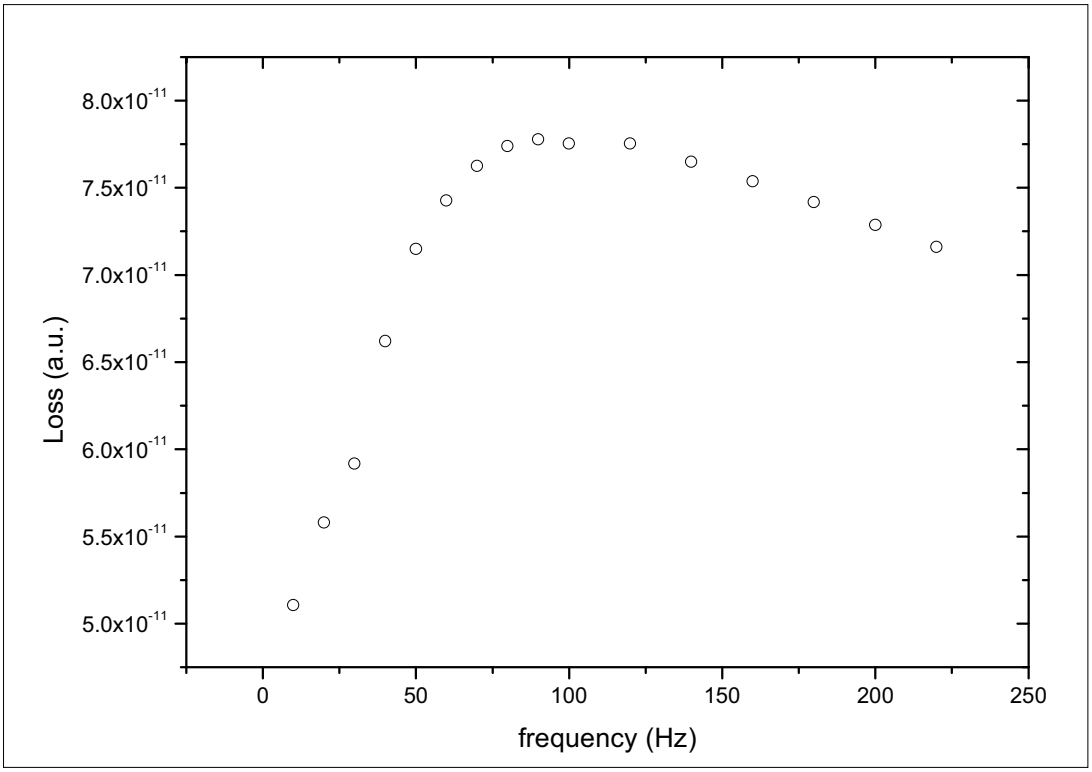

Figure 5.1 Loss vs. frequency diagram for 20mm length of 0.18mm thick tape

In Figure 5.1 the *Q-f* for the 20mm sample is presented. The diagram fits the Campbell model of coupling loss (Figure 3.2) which means that the Campbell equation (Eq 3.9) can be applied to our measurements. In the diagram the peak frequency appears at f=90Hz and an uncertainty of the measured loss for the frequency is estimated as σ_f =10Hz.

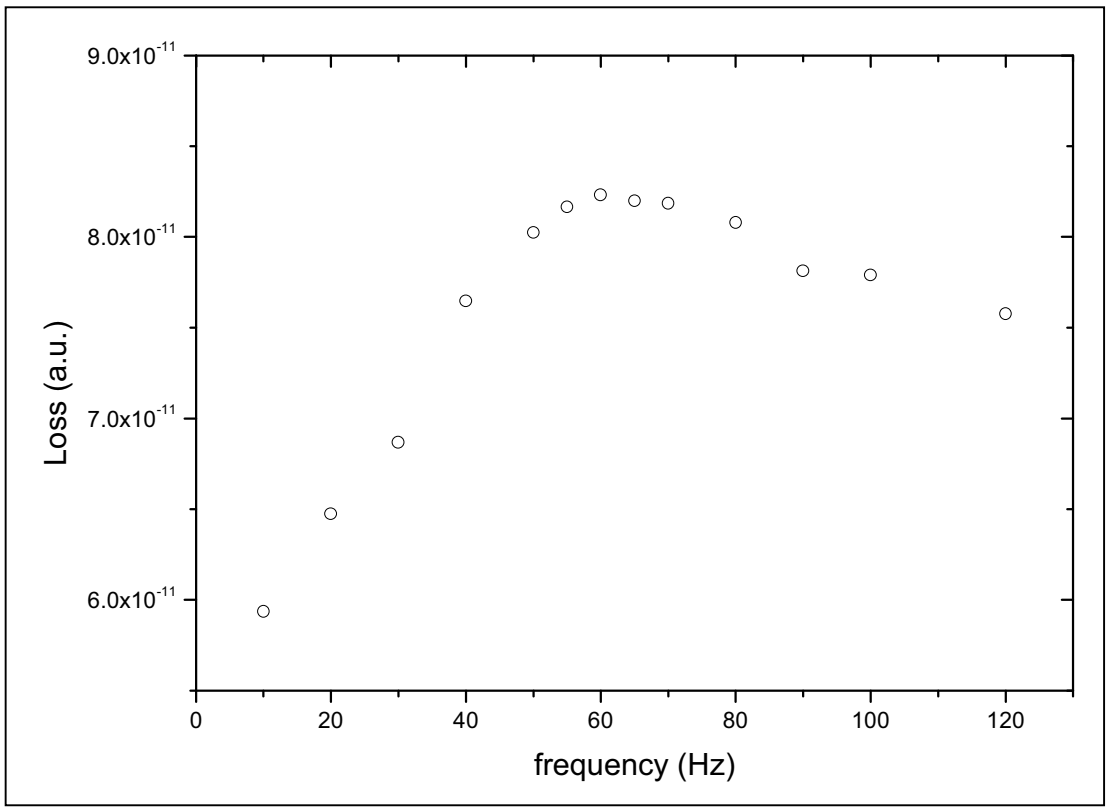

Figure 5.2 Loss vs. frequency diagram for 24mm length of 0.18mm thick tape

In Figure 5.2 the *Q-f* for the 24mm sample is presented. The diagram fits the Campbell model of coupling loss (Figure 3.2) which means that the Campbell equation (Eq 3.9) can be applied to our measurements. In the diagram the peak frequency appears at *f*=60Hz and an uncertainty of the measured loss for the frequency is estimated as σ_f=5Hz.

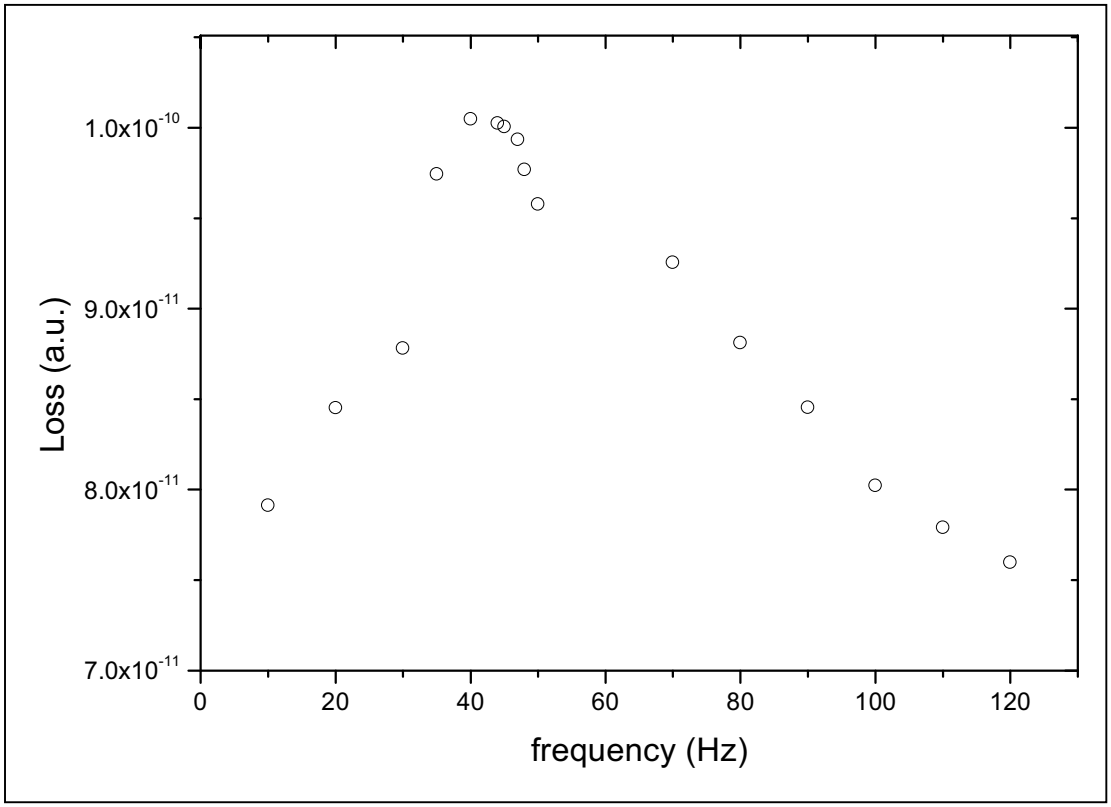

Figure 5.3 Loss vs. frequency diagram for 28mm length of 0.18mm thick tape

In Figure 5.3 the *Q-f* for the 28mm sample is presented. The diagram fits the Campbell model of coupling loss (Figure 3.2) which means that the Campbell equation (Eq 3.9) can be applied to our measurements. In the diagram the peak frequency appears at *f*=40Hz and an uncertainty of the measured loss for the frequency is estimated as σ_f =5Hz.

5.1.2 0.24mm Thickness

The 0.24mm thickness tape was cut to three lengths of 20mm, 22mm, and 26mm. For each length the Q-*f* diagram is plotted (Figures 5.4, 5.5, 5.6)

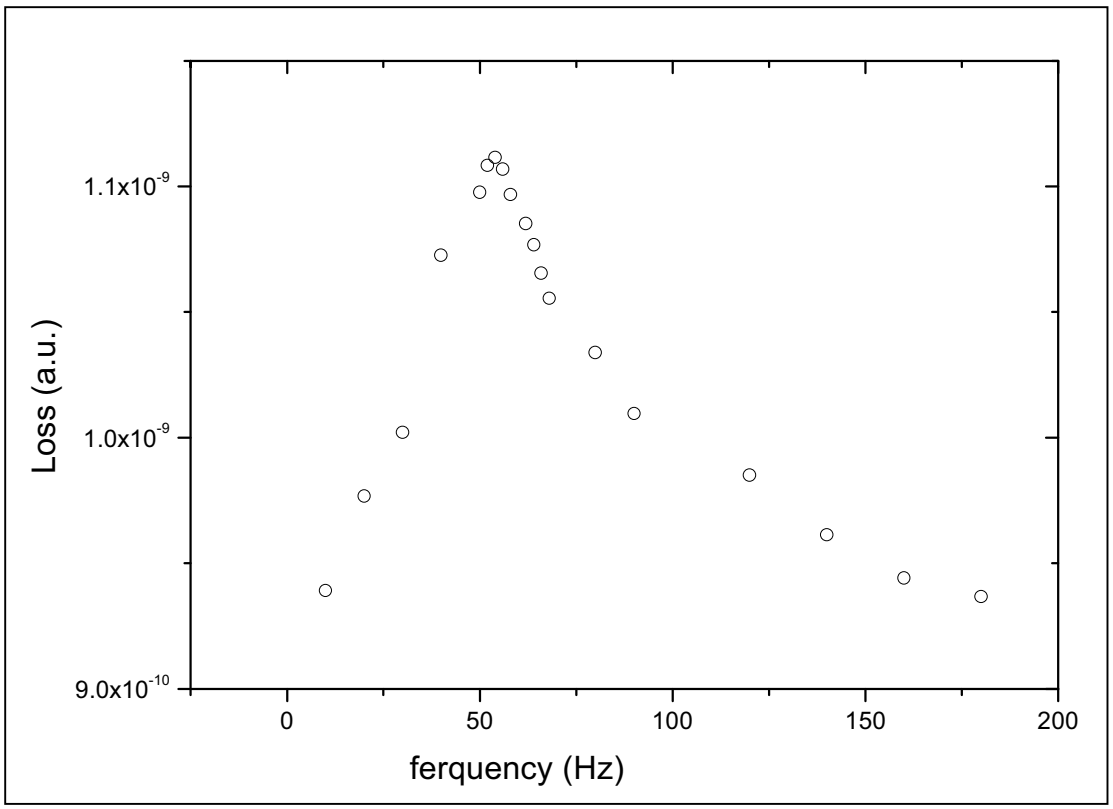

Figure 5.4 Loss vs. frequency diagram for 20mm length of 0.24mm thick tape

In Figure 5.4 the *Q-f* for the 20mm sample is presented. The diagram fits the Campbell model of coupling loss (Figure 3.2) which means that the Campbell equation (Eq 3.9) can be applied to our measurements. In the diagram the peak frequency appears at *f*=54Hz and an uncertainty of the measured loss for the frequency is estimated as σ_f =1Hz.

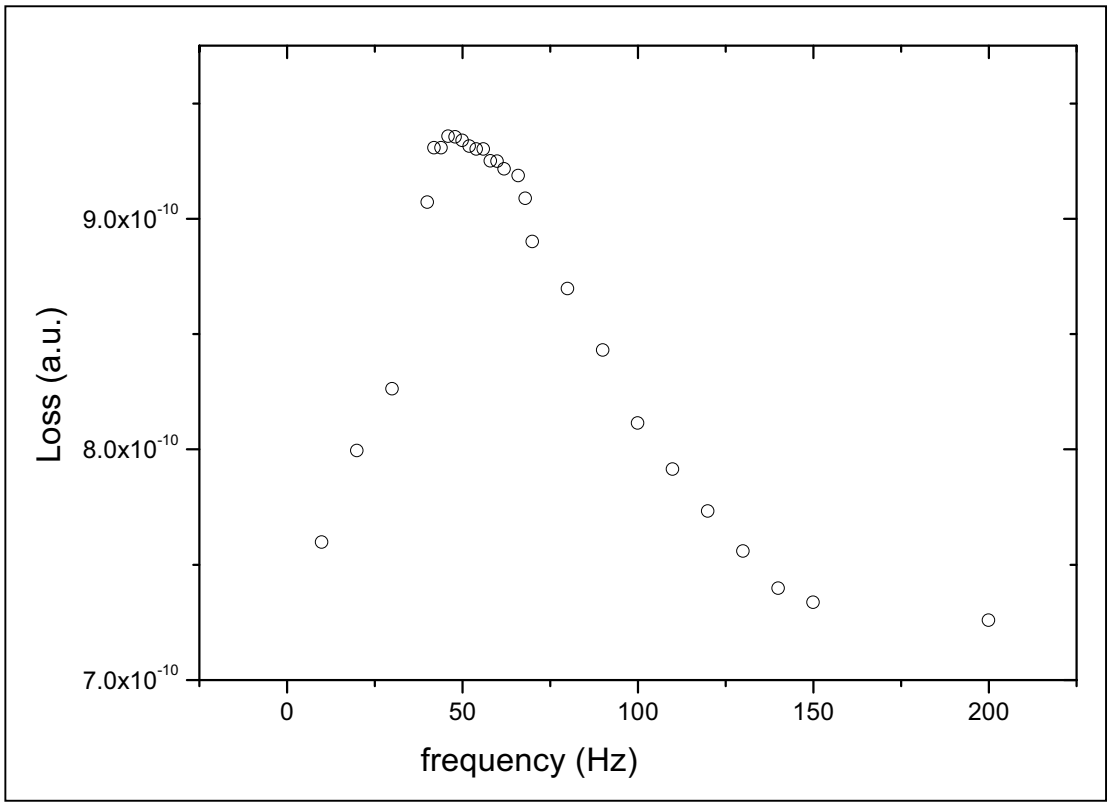

Figure 5.5 Loss vs. frequency diagram for 22mm length of 0.24mm thick tape

In Figure 5.5 the *Q-f* for the 22mm sample is presented. The diagram fits the Campbell model of coupling loss (Figure 3.2) which means that the Campbell equation (Eq 3.9) can be applied to our measurements. In the diagram the peak frequency appears at f=46Hz and an uncertainty of the measured loss for the frequency is estimated as σ_f =10Hz.

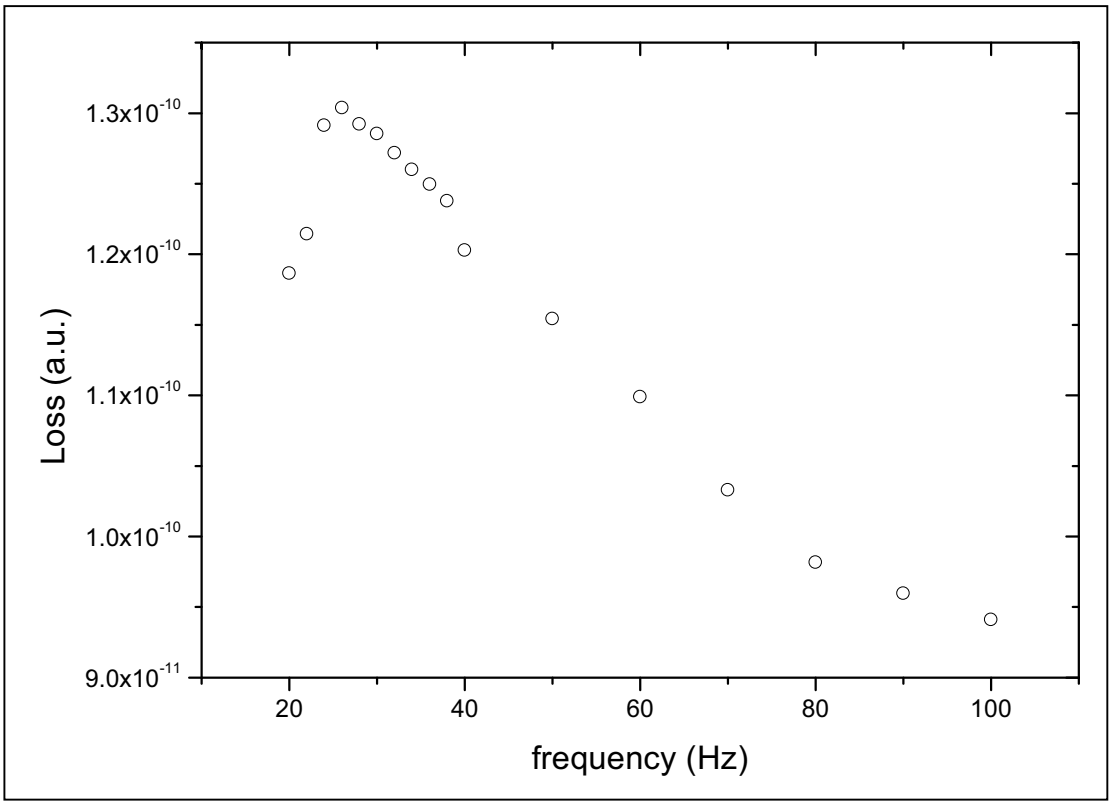

Figure 5.6 Loss vs. frequency diagram for 26mm length of 0.24mm thick tape

In Figure 5.6 the *Q-f* for the 26mm sample is presented. The diagram fits the Campbell model of coupling loss (Figure 3.2) which means that the Campbell equation (Eq 3.9) can be applied to our measurements. In the diagram the peak frequency appears at *f*=26Hz and an uncertainty of the measured loss for the frequency is estimated as σ_f =5Hz.

5.1.3 0.33mm Thickness

The 0.33mm thickness tape was cut to three lengths of 21mm, 24mm, and 26mm. For each length the *Q-f* diagram is plotted (Figures 5.7, 5.8, 5.9)

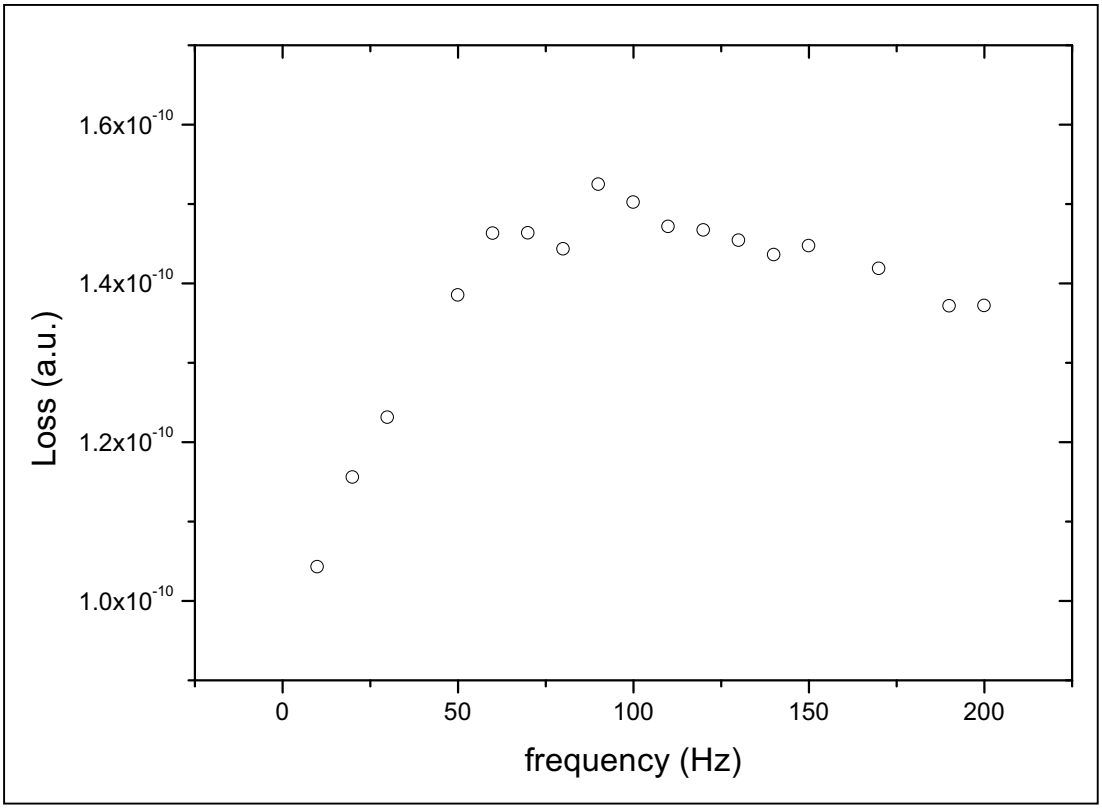

Figure 5.7 Loss vs. frequency diagram for 21mm length of 0.33mm thick tape

In Figure 5.7 the *Q-f* for the 21mm sample is presented. The diagram fits the Campbell model of coupling loss (Figure 3.2) which means that the Campbell equation (Eq 3.9) can be applied to our measurements. In the diagram the peak frequency appears at *f*=90Hz and an uncertainty of the measured loss for the frequency is estimated as σ_f=10Hz.

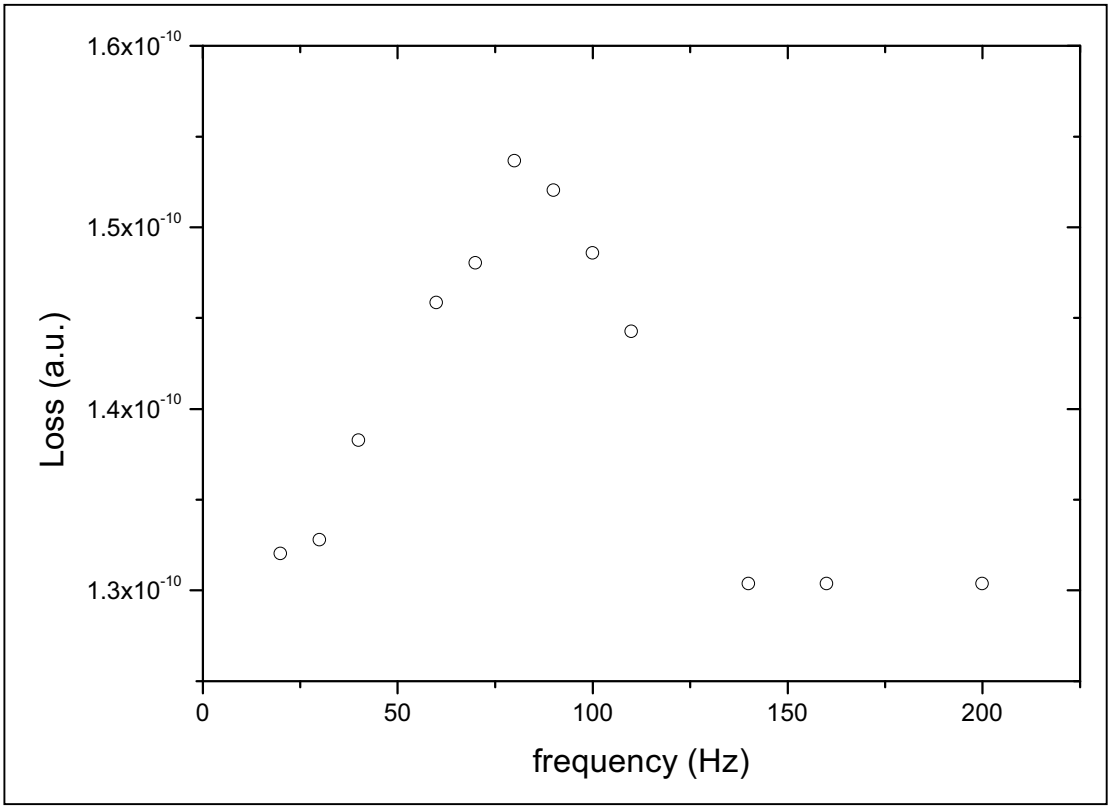

Figure 5.8 Loss vs. frequency diagram for 24mm length of 0.33mm thick tape

In Figure 5.8 the *Q-f* for the 24mm sample is presented. The diagram fits the Campbell model of coupling loss (Figure 3.2) which means that the Campbell equation (Eq 3.9) can be applied to our measurements. In the diagram the peak frequency appears at f=80Hz and an uncertainty of the measured loss for the frequency is estimated as σ_f=5Hz.

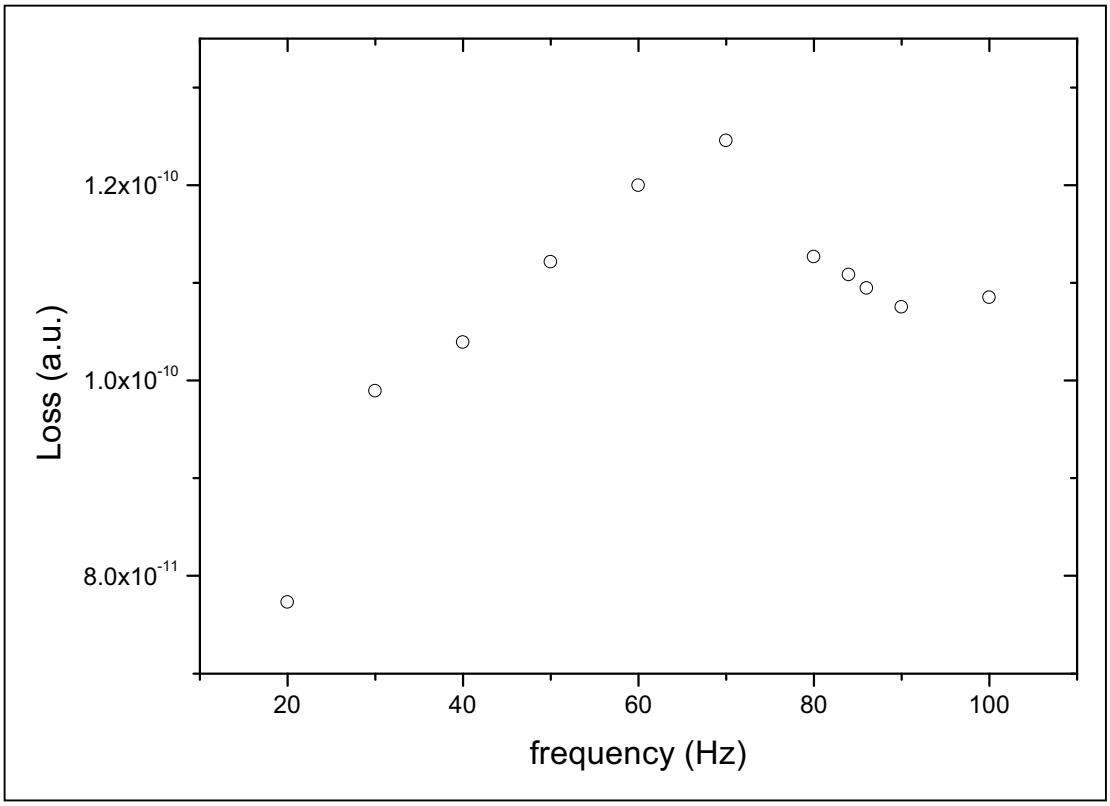

Figure 5.9 Loss vs. frequency diagram for 26mm length of 0.33mm thick tape

In Figure 5.9 the *Q-f* for the 26mm sample is presented. The diagram fits the Campbell model of coupling loss (Figure 3.2) which means that the Campbell equation (Eq 3.9) can be applied to our measurements. In the diagram the peak frequency appears at f=70Hz and an uncertainty of the measured loss for the frequency is estimated as σ_f =5Hz.

5.2 Analysis of the Tapes

As explained earlier, the value of τ can be obtained from Q- *f* curve, since $\omega\tau$=1 for the peak frequency. Referring to Sections 5.1.1, 5.1.2 and 5.1.3 along with obtained Q-*f* diagrams, shows that all *Q-f* diagrams satisfy the Campbell model (Section3.2). The $\rho_{\perp}$ value of each diagram can be obtained using Eq 3.9.

The $\rho_{\perp}$ value is calculated by taking $\omega\tau$=1 in each diagram. An uncertainty $\sigma_{\rho_{\perp}}$, for $\rho_{\perp}$ is estimated (Eq 5.1) for each Q-*f* diagram due to the measuring method used in the experiments:

$$\sigma_{\rho_{\perp}} = \sqrt{\left(\frac{\partial\rho}{\partial L^2}\right)\sigma_{L^2} + \left(\frac{\partial\rho}{\partial f}\right)\sigma_f} \qquad \textbf{Eq 5.1}$$

For each diagram, uncertainty values of σ_f and σ_{L^2} were also estimated relating to *f* and L^2 respectively. The results are illustrated in Table 5.1 for each sample.

Table 5.1 The numerical results obtained from the *Q-f* diagram plotted for each length and tape thickness

Number of filaments	Thickness (a) (cm)	Width (b) (cm)	Length (L) (cm)	σ_{L^2} (cm^2)	*f* (Hz)	σ_f (Hz)	$\rho_{\perp}$ (Ωcm)
8 filaments	0.018	0.396	2.0	0.4	90	10	1.44×10^{-6}
			2.4	0.48	60	5	1.38×10^{-6}
			2.8	0.56	40	5	1.25×10^{-6}
	0.024	0.443	2.0	0.4	54	1	8.64×10^{-7}
			2.2	0.44	46	10	8.91×10^{-7}
			2.6	0.52	26	5	7.03×10^{-7}
	0.033	0.524	2.1	0.42	90	10	1.59×10^{-6}
			2.4	0.48	80	5	1.84×10^{-6}
			2.6	0.52	70	5	1.89×01^{-6}

Using the results in Table 5.1 for ρ and L^2 values along with σ_f and σ_{L^2} as error bars, a $\rho_\perp$-L^2 diagram is obtained for each sample thickness, which is shown in Figure 5.10 to 5.12.

The experimental data are not accurate enough to show proportionality between $\rho_\perp$ and L^2. The length of the tape would have to vary much more than for the measured tapes, which would not be possible to measure with the available set-up.

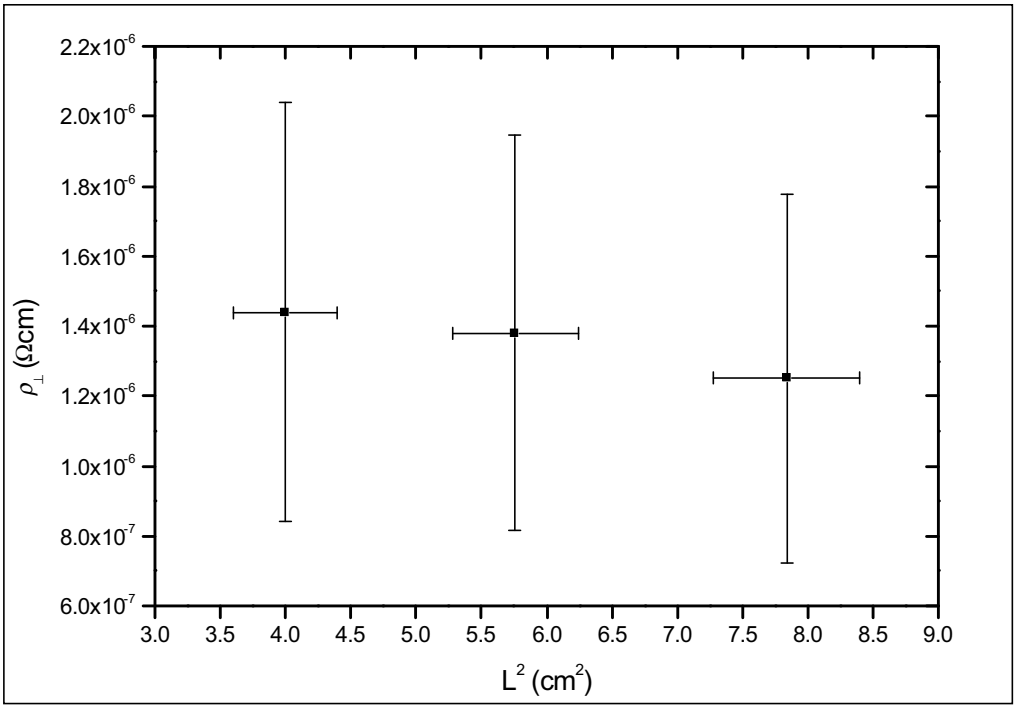

Figure 5.10 $\rho_\perp$-L^2 diagram for 0.18mm thickness tape

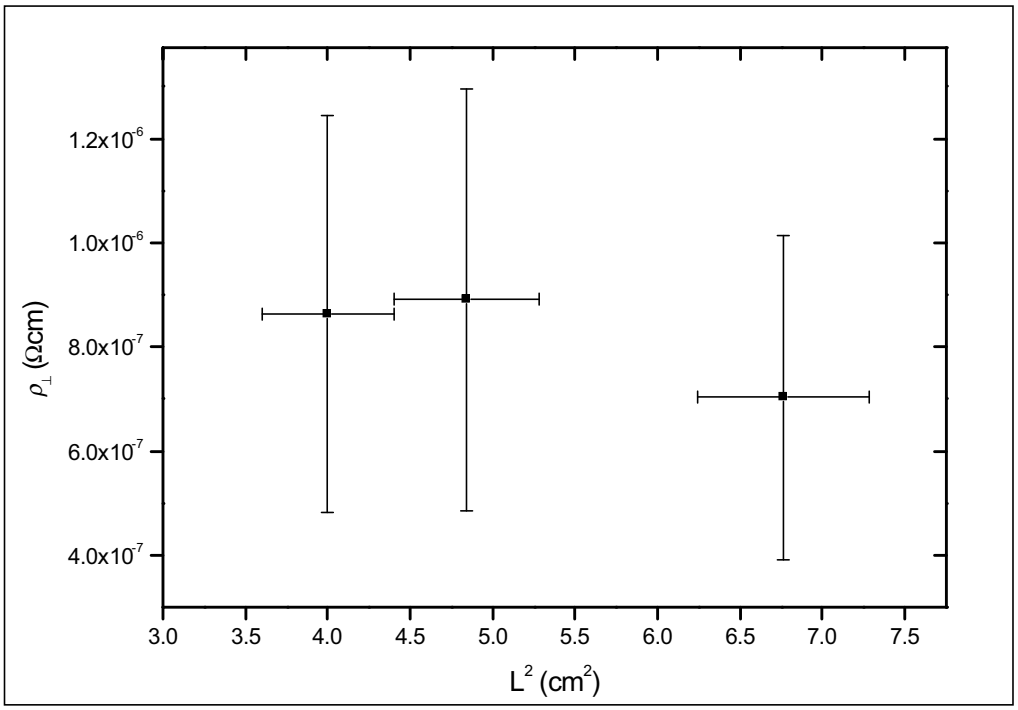

Figure 5.11 $\rho_{\perp}$-L^2 diagram for 0.24mm thickness tape

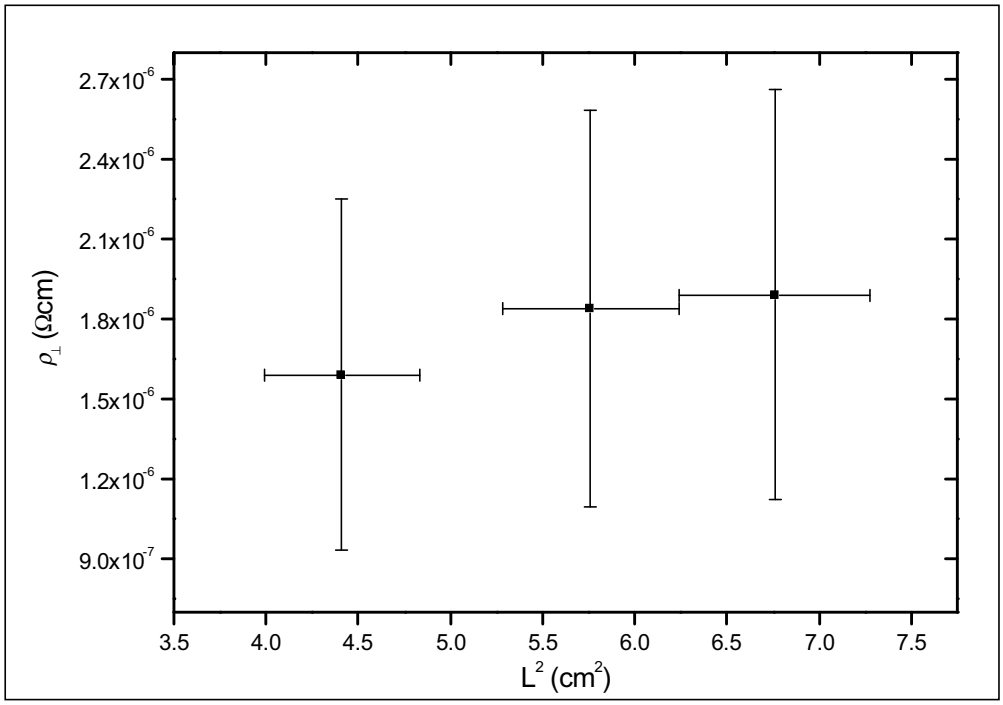

Figure 5.12 $\rho_{\perp}$-L^2 diagram for 0.33mm thickness tape

According to Block-Grüneisen theory, $\rho_{\perp}$ should be independent of the shape factor n and then the $\rho_{\perp}$-n diagram for each thickness should be a horizontal line. In order to plot $\rho_{\perp}$-n diagram, the average value of $\rho_{\perp}$ is obtained for each thickness (Table 5.1) and an uncertainty for $\rho_{\perp}$ is computed using the calculated average amount of $\rho_{\perp}$ for each thickness-length of tape. The results are illustrated in Table 5.2. It is also necessary to estimate the uncertainty of n which is:

$$\sigma_n = \sqrt{\left(\frac{\partial n}{\partial a}\right)^2 \sigma_a^2 + \left(\frac{\partial n}{\partial b}\right)^2 \sigma_b^2} \qquad \textbf{Eq 5.4}$$

The measurement of a and b is achieved by using a micrometer with an accuracy of 0.001cm, then $\sigma_a = \sigma_b = \pm 0.001 cm$

$$\sigma_n = (0.001)\sqrt{\left(\frac{a^2 + b^2}{b^4}\right)}$$

Table 5.2 Data collected from $\rho_{\perp average}$-n diagrams for different thicknesses of 8 filament tapes

Thickness (cm)	Width (cm)	n (a/b)	Length (cm)	σ_n	$\rho_{\perp average}$ (Ωcm)	$\sigma_{\rho_{\perp average}}$ (Ωcm)
0.018	0.396	0.05	2.0	2.53×10^{-3}	1.4×10^{-6}	1×10^{-7}
			2.4			
			2.8			
0.024	0.443	0.054	2.0	2.26×10^{-3}	8.2×10^{-7}	1×10^{-7}
			2.2			
			2.6			
0.033	0.524	0.63	2.1	1.91×10^{-3}	1.8×10^{-6}	2×10^{-7}
			2.4			
			2.6			

By using the data in Table 5.2, the $\rho_{\perp average}$-n diagram is plotted as shown in Figure 5.13. The Figure shows that $\rho_{\perp}$ is not independent of the tape thickness.

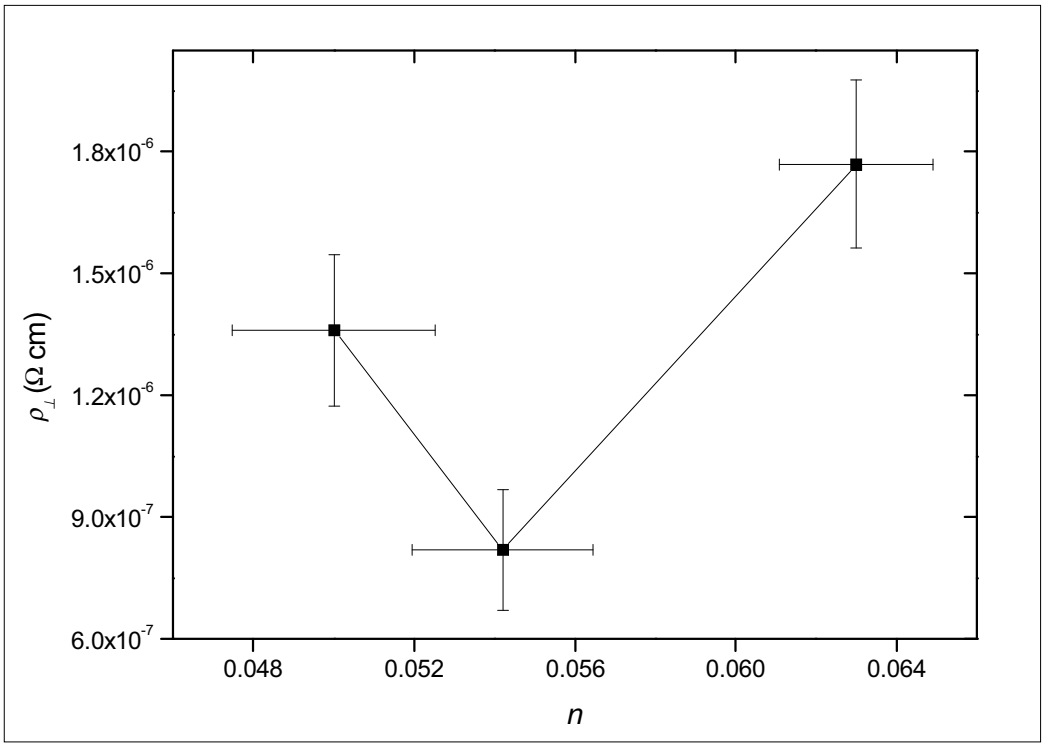

Figure 5.13 $\rho_{\perp average}$ vs. shape factor for three different tape of 8 filament

The matrix resistivity, ρ_{Ag}, is measured at 77K [13, 28] and was reported to be of the order of $\sim 10^{-7}\,\Omega$cm. $\rho_{\perp}$ is compared to ρ_{Ag} in Table 5.3.

Table 5.3 Comparison of $\rho_{\perp}$ with ρ_{Ag} at 77K

Shape factor	Length (cm)	$\rho_{\perp}$ (cm)	$\rho_{\perp} / \rho_{Ag}$
0.05	2	1.44×10^{-6}	5.14
	2.4	1.38×10^{-6}	4.94
	2.8	1.25×10^{-6}	4.48
0.054	2	8.64×10^{-7}	3.09
	2.2	8.91×10^{-7}	3.18
	2.6	7.03×10^{-7}	2.51
0.063	2.1	1.59×10^{-6}	5.67
	2.4	1.84×10^{-6}	6.58
	2.6	1.89×10^{-6}	6.76

From Table 5.3 it is evident that $\rho_{\perp}$ is larger than what is expected, which could be explained by Block-Grüneisen theory.

Chapter 6

Conclusion

In this research nine pieces of 8-filament HTS tape of different lengths and thicknesses were studied. Throughout the work, I_c, XRD, and optical microscopy were used to study the sample, and then magnetic hysteresis loop was obtained in order to calculate $\rho_\perp$.

The results from XRD and critical current measurements tend to show a good agreement. The obtained values of the critical current are related to the percentage of Bi-2223 after sintering.

The optical microscope images show that there is neither bridging nor discontinuities of the filaments, which indicates to reliable tapes for the measurements.

The I_c vs. thickness curve (Figure 4.5) and the ρ vs. thickness curve (Figure 5.13) are obtained. Comparing these two diagrams shows no apparent correlation between I_c and $\rho_\perp$.

The calculated $\rho_\perp$ values for all 9 samples (Table 5.1) give $\rho_{\perp average}=1.3\pm0.4\mu\Omega cm$. However, $\rho_\perp$ is significantly larger than ρ_{Ag} of the sample matrix (Table 5.3). According to Block-Grüneisen theory this is due to the presence of flux creep in the samples.

It would be very interesting to repeat the measurements with the field perpendicular to the tape. It is expected the time relation should be independent from the shape factor, n, and a different τ and hence $\rho_\perp$ would be obtained in response to the change in coupling-current path.

References

1- P.V.P.S.S. Sastry, K.M.Amm, D.C.Knoll, S.C.Peterson , J.Schwartz, *Physica C* **297** (1998) p223
2- H. Shaked, P. M. Keane, J. C. Rodriguez, F. F. Owen, R. L. Hitterman, J. D. Jorgensen, *Crystal structures of the high-Tc superconducting copper-oxides*, Elsevier Science B. V., 1994
3- J. G. Bednorz and K. A. Müller, Z, *Phys. B* **64** (1986)p189
4- M. K. Wu, J.R. Ashburn, C. J. Torng, P. H. Hor, R. L. Meng, L. Gao, Z. J. Huang, Y. Q. Wang and C. W. Chu, *Phys. Rev. Lett*. **58** (1987) p908
5- H. Maeda, Y. Tanaka, M. Fukutomi and T. Asano, *Japan. J. Appl. Phys.* **27** (1988) pL209
6- WTEC Panel Report on: *Power Applications of Superconductivity in Japan and Germany*, Sep 1997, Loyola College, Maryland, USA
7- C.P.Bean, *Physic Review Letter*, **8** (1962) p250
8- J. R. Clem, *Physica C* **162-164** (1989) p1137
9- J. R. Clem, *Phys. Rev. B* **43** (1991) p7837
10- M. E. Gaevski, A. V. Bobyl, and D. V. Shantsev, *Physical Revies B,* **59** (1999) p9655
11- M.N. Wilson, *Superconducting Magnets, Monograph on Cryogenics*, Clarendon Press, Oxford, 1983
12- W.J. Carr, *AC Loss and Macroscopic Theory of Superconductors*, Hordon and Breach Science Publisher, 1983
13- K. Kwasnitza, St. Clerc, *Physica C* **233** (1994) p423
14- St. Clerc Thesis ETH-Zurich Switzerland, Diss ETH No.11353, 1995
15- K. Funaki, K. Kajikawa, H. Tomiya, M. Nakamura, M.Iwakuma, S. Miyake, T. Kumano, *Adv. Cryo. Eng.* **43** (1998) to be published
16- K.V.Namjoshi, P.P.Biringer*, IEEE Trans. on Magnetics* **24** (1988) p2181
17- K.Kwasbutza, *Cryogenics* **17** (1977) p617
18- A.M.Campbell, *Cryogenics* **22** (1982) p3
19- W.J. Carr, *AC Loss and Macroscopic Theory of Superconductors*, Hordon and Breach Science Publisher, 1983
20- M.D.Sumption, E.Lee, E.W.Collings, *Physica C* **337** (2000) p187
21- M.D.Sumption, E.Lee, S.X.Dou, E.W.Collings, *Physica C* **335** (2000) p164
22- E.W.Collings, M.D.Sumption,*The 13th Symposium on Superconductivity,* ISS 2000, Tokyo, Japan
23- E.W.Collings, private communication whit E.W.Collings, 2002
24- C.Kittel, *Introduction to solid stsat physics*, 2nd edition, John Wiely & Sons, 1956
25- W.G.Wang, H.K.Liu, Y.C.Guo, P.Bain, S.X.Dou, *Appl. Superconductor* **3(11-12)** (1995) p599
26- Q.Y.Hu, H.K.Liu, S.X.Dou, *Physica C* **250** (1995) p7
27- M.Polak, L.Krempasky, *Physica C.* **357-360** (2001) p1144

Summary

An 8-filament Bi-2223/Ag wire was produced by the PIT method from 16gr powder in a 20cm silver tube. Sections of the wire were drawn/rolled to 0.18mm, 0.24mm, and 0.33mm thickness without any bridging between the filaments. The tapes were heat treated with two-step sintering at 837^{o}C and an intermediate pressing between the two sintering. Optical Microscopic test was taken to confirm no bridging between the filaments at the final stage of the tape preparation process. The tapes were examined by XRD which showed that the percentage of Bi-2223 as compared to Bi-2212 was X_{Bi2223}= ~87%.

In order to calculate the AC loss, the tapes were exposed to a parallel AC magnetic field. The experimental set-up was made at University of Wollongong.

The Q-*f* diagrams for the tape samples were obtained experimentally. Considering $\omega\tau$=1 at the peak point of the Q-*f* diagram, the value of the peak frequency, f_c, was obtained for each Q-*f* diagram. Using Carr's modified equation $\rho_{\perp} = (4/10^9)L^2 f_c$, the value of $\rho_{\perp}$ was numerically obtained for each length-thickness of the samples and $\rho_{\perp}$ vs. thickness diagram constructed accordingly. $\rho_{\perp}$ does vary significantly with thickness and is also large, comparing to ρ_{Ag} of the tape matrix. This could be attributed to the presence of flux creep which was explained by Block-Grüneisen theory. The average $\rho_{\perp}$ for the 9 samples was: $\rho_{\perp average}$=1.3±0.4$\mu\Omega cm$.

The critical current, I_c, was also measured for each thickness of tape. The results are summarised in Table S.1.

Table S.1 Measured values of I_c, collected values of τ, and obtained values of $\rho_\perp$ for different samples of 8 filament tapes

Number of filaments	Thickness (cm)	Width (cm)	I_c (A)	Length (cm)	f_c (Hz)	$\rho_\perp$ (Ωcm)
8 filaments	0.018	0.396	11.2	2	90	1.44×10^{-6}
				2.4	60	1.38×10^{-6}
				2.8	40	1.25×10^{-6}
	0.024	0.443	17.85	2	54	8.64×10^{-7}
				2.2	46	8.91×10^{-7}
				2.6	26	7.03×10^{-7}
	0.033	0.524	13.8	2.1	90	1.59×10^{-6}
				2.4	80	1.84×10^{-6}
				2.6	70	1.89×01^{-6}

Acknowledgement

I would like to express my sincere gratitude to my parents, my wife and my sister for their sincere support during my research. I wish particularly to distinguish the dedication of my parents to me, which was my main source of encouragement in my whole life of education. Financial supports of my father made my studies possible.

I would like also to extend my sincere appreciation to my supervisors, Prof. S.X.Dou and J.Horvat for their academic guidance, financial support and continues encouragement throughout the project. I would also like to express my sincere thanks to, T. Silver, M. Ionescu and X. L. Wang for their assistance, comments on the manuscript and during the project. Horvat, Ionescu and Wang also helped in performing the experiments and with discussions.

Many thanks to all of the members of the Institute of Superconducting and Electronic Materials, and to all technicians at the Department of Materials Engineering. Thanks also go to Mrs. B. Allen for her help in office matters.